



Facile construction of new coronal-like MnCeO_x hollow nanosphere for efficiently removing o-dichlorobenzene



Weitong Ling^{a,b}, Peng Gao^b, Wenyuan Du^c, Shilin Wu^a, Haijun Zhao^{a,d,*}, Fang Dong^a, Fei Zha^{b,**}, Zhicheng Tang^{a,d,*}

^a State Key Laboratory for Oxo Synthesis and Selective Oxidation, and National Engineering Research Center for Fine Petrochemical Intermediates, Lanzhou Institute of Chemical Physics, Chinese Academy of Sciences, Lanzhou 730000, China

^b College of Chemistry and Chemical Engineering, Northwest Normal University, Lanzhou 730070, China

^c Shanghai Key Lab of Chemical Assessment and Sustainability, School of Chemical Science and Engineering, Tongji University, Shanghai 200092, PR China

^d Yantai Zhongke Research Institute of Advanced Materials and Green Chemical Engineering, Shandong Laboratory of Yantai Advanced Materials and Green Manufacturing, Yantai 264006, China

ARTICLE INFO

Keywords:

New-coronal like
Mn-Ce interaction
O-dichlorobenzene
Oxygen vacancy
Reaction mechanism

ABSTRACT

Designing unique and ingenious microstructure or morphology of catalysts is critical and still a challenge to obtain high catalytic performance in catalytic combustion reactions under dry air and 5.0 vol% H_2O conditions, especially by economic and efficient measures. In pursuit of this goal, a facile strategy was exploited to accurately construct new-coronal like MnCeO_x hollow microsphere with different Ce contents. This unique structure can expose more active sites and has excellent redox ability. The simulation results of generalized gradient approximation (GGA) of density functional theory (DFT) indicated that the introduction of a certain amount of Ce can effectively improve the adsorption and activation of o-DCB molecules on Mn_3O_4 . The detailed study showed that the $\text{Mn}_2\text{Ce}_1\text{O}_x$ hollow nanosphere exhibited excellent catalytic performance in the presence of 5.0 vol% H_2O . Ideally, the action of Marse-van Krevelen (Mvk) combine Langmuir-Hinshelwood (L-H) mechanism was deduced based on the origin of oxygen species under dry air conditions. In general, the green and facile synthetic strategy provides a new idea for the design of hollow microsphere Mn-based catalyst and the unique structure significantly improves the comprehensive performance of o-DCB catalytic oxidation, which brings great hope for industrial application.

1. Introduction

The emission of volatile organic compounds (VOCs) has brought many environmental problems [1]. Such as photochemical smog, production of ozone and global warming [2]. It is incredibly harmful to human beings due to its vigorous carcinogenic activity and highly toxic pollutants, especially for chlorine containing volatile organic compounds (C VOCs or Cl-VOCs) [3,4]. Therefore, it is essential to eliminate the organic waste gas at low temperature. Among many elimination technologies, catalytic combustion has a better elimination effect and lower operating temperature and is considered a very potential means [5,6]. In addition, taking into account the fine manipulation in the laboratory, model compounds are used to evaluate the activity of the

catalysts in most of these studies, and o-dichlorobenzene (o-DCB) is often used as a gas model to evaluate catalytic performance [7]. Catalysts play a significant role in the catalytic elimination of C VOCs. In particular, metal catalysts have been widely used. Generally speaking, metal catalysts include noble metal catalysts and transition metal catalysts. Precious metals usually exhibit excellent properties, but their wide range of applications is limited by the high price. Therefore, transition metal catalysts have attracted more and more attention due to their remarkable catalytic performance and low cost [8–11]. Recently, transition metal oxides, such as MnO_x , Co_3O_4 , CeO_2 and Fe_2O_3 show an excellent catalytic performance in eliminating the C VOCs at low temperature [12–15]. Among the above oxides, MnO_x is considered as one of the promising catalysts because of their excellent redox performance,

* Corresponding authors at: State Key Laboratory for Oxo Synthesis and Selective Oxidation, and National Engineering Research Center for Fine Petrochemical Intermediates, Lanzhou Institute of Chemical Physics, Chinese Academy of Sciences, Lanzhou 730000, China

** Corresponding author.

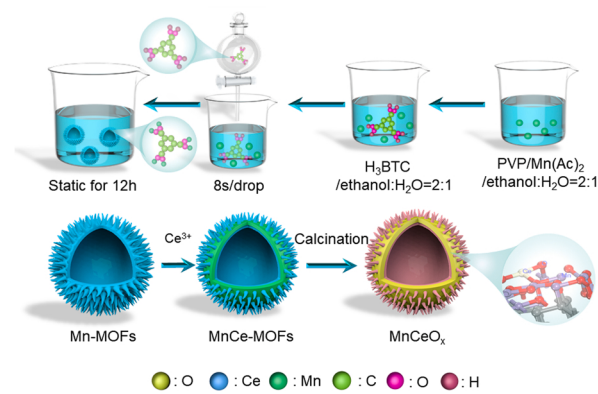
E-mail addresses: zhaihaijun@licp.ac.cn (H. Zhao), zhafei@nwnu.edu.cn (F. Zha), tangzhicheng@licp.ac.cn (Z. Tang).

which is mainly due to the structural characteristics of Mn and the good fitness of the environment [16,17]. However, the redox ability of single metal oxide (MnO_x) is often limited, and its stability is not ideal [18,19]. Therefore, it is particularly important to improve the chlorine resistance and redox ability of manganese oxides by modifying MnO_x based catalysts. When a transition metal oxide is introduced, the synergistic effect between them can be promoted, and the catalytic performance of binary transition metal compound catalyst can be further improved. CeO_2 has attracted more and more attention in recent years because of its excellent oxygen storage and release capacity for the catalytic oxidation of CVOCs [20]. Xing et al. found that the superficial interaction between Mn and Ce can produce Mn^{4+} and oxygen vacancies on the $\text{Ce}/\text{Mn-NF}$ catalysts, which significantly improved the redox capacity of the $\text{Ce}/\text{Mn-NF}$ catalyst [21].

As everyone knows that the microstructure and morphology of catalysts play an essential role in catalytic performance, which is called “structure and morphology action” [16]. In the past research process, people successfully synthesized MnO_x with different morphologies, including nanorods, nanotubes, nanosheets and microspheres, and hierarchical structures [22–26]. However, a hollow hierarchical structure has been proven to be a potent catalyst structure because of its high specific surface area and exposure to more active sites. Zhao et. al reported the synthesizing of hollow-structured MnO_x and $\text{FeO}_x\text{-MnO}_x$ samples by the self-template route and applied for CO oxidation. The results showed that high specific surface area and strong redox ability were essential for excellent catalytic performance [27]. Chen et. al reported the synthesized Mn_2O_3 hollow microspheres ($\text{Mn}_2\text{O}_3\text{-HMS}$) through the traditional hydrothermal method for the first time. The results showed that the unique structure could shorten the diffusion pathways of electrons and ions and provide rich redox sites for high-performance supercapacitors [28]. Building advanced systems to improve catalytic performance is extremely challenging [29]. In general, MnO_x hollow microspheres prepared by traditional methods inevitably face many problems, such as cumbersome synthesis processes and energy consumption. However, the green and convenient synthesis strategy not only overcomes these problems, but also has the potential for industrialization.

Metal Organic Frameworks (MOFs) have potential application prospects in various fields due to their unique architecture and function [30–32]. MOFs has been regarded as precursors for thermal decomposition to synthesize transition metal oxide catalysts, and the reason is that the annealed transition metal oxides can not only maintain the morphology and some physical and chemical properties of MOFs precursors, but also obtain uniformly distributed ultrafine metal oxide nanoparticles. In recent years, more and more studies have shown that the structure of MOFs can be regulated in many ways [33]. Given the advantages of hollow structure, the design and synthesis of hollow MOFs have attracted a lot of research interest and people have made ongoing efforts to explore this research. Recently, we found that the conventional synthesis methods for building hollow structures are mainly template methods, including external and internal template methods. These methods are cumbersome, complex and energy consuming, and how to synthesize MOFs with hollow structures directly in one step is still a serious challenge. Considering these aspects, and inspiration about the MOFs with hollow microspheres structure is synthesized by green and facile synthetic strategy emerged in our mind (Scheme 1).

Herein, we proposed a facile synthesis strategy to a series of new coronal-like Ce-doped MnO_x hollow nanosphere derived from MnCe -MOFs (Scheme 1) were evaluated in the catalytic oxidation reaction of o-DCB. The resultant $\text{Mn}_2\text{Ce}_1\text{O}_x$ (catalyst with Mn and Ce incorporation ratio is 2:1) exhibited high catalytic performance under dry air ($T_{90} = 335^\circ\text{C}$) and 5.0 vol% H_2O ($T_{90} = 365^\circ\text{C}$) conditions. Experimental results and GGA of DFT indicate that the Ce content has a wide influence on the micro morphology, crystal structure of MnCeO_x , and adsorption and activation of o-DCB molecules. Meanwhile, the unique special structure exposes more active components, oxygen vacancies, excellent



Scheme 1. Fabrication diagram of fabrication of new coronal-like hollow microspheres MnCeO_x catalysts.

redox ability and rich acid sites, which jointly promote the catalytic ability of $\text{Mn}_2\text{Ce}_1\text{O}_x$. What's more, degradation mechanism based on the source of reactive oxygen species has been deeply studied.

2. Experimental section

2.1. Catalysts preparation

2.1.1. Synthesis of Mn-MOFs

Typically, 2 mmol of $\text{Mn}(\text{OAc})_2\cdot 4\text{H}_2\text{O}$ and 2 g of polyvinylpyrrolidone (PVP) were dissolved in 100 mL mixed solution of ethanol and deionized water ($V_{\text{ethanol}}:V_{\text{water}} = 2:1$) to form solution A. 0.9 g of 1,3,5-benzoic acid was dissolved into the similar mixed solution to form solution B. The solution B was slowly dropped into solution A and allowed to stand for 12 h. Then the white precipitate was collected after washed 3 times with methanol, centrifuged and dried in a vacuum oven at 80°C for 12 h. The obtained sample was marked as Mn-MOFs.

2.1.2. Synthesis of new coronal-like MnCeO_x hollow nanosphere

MnCeO_x catalysts were prepared as the following process. The Mn-MOFs were firstly dispersed into 60 mL ethanol containing 0.3 and 1 mmol of $\text{Ce}(\text{NO}_3)_3\cdot 6\text{H}_2\text{O}$, respectively, with ultrasonic for 30 min. Then it was stirred for 1 h at room temperature, and finally washed 3 times with methanol and dried. The obtained samples were labeled $\text{Mn}_3\text{Ce}_1\text{-MOFs}$ and $\text{Mn}_2\text{Ce}_1\text{-MOFs}$, respectively. At last, the Mn-MOFs, $\text{Mn}_3\text{Ce}_1\text{-MOFs}$ and $\text{Mn}_2\text{Ce}_1\text{-MOFs}$ samples were calcined at 450°C for 3 h to obtain MnO_x , $\text{Mn}_3\text{Ce}_1\text{O}_x$ and $\text{Mn}_2\text{Ce}_1\text{O}_x$ catalysts, respectively.

2.2. Catalyst characterization

The structure and performance analysis of a series of catalysts were shown in the [supporting information](#).

2.3. Catalytic tests

The catalytic performance test for the catalytic oxidation of o-DCB on the catalyst was listed in the [supporting information](#).

3. Results and discussion

3.1. Study of the samples by electron microscopy

Intuitively, Mn-MOFs, $\text{Mn}_3\text{Ce}_1\text{-MOFs}$, and $\text{Mn}_2\text{Ce}_1\text{-MOFs}$ are detected using scanning electron microscopy (SEM) techniques. Mn-MOFs mainly demonstrate the morphology of small spheres with a hollow structure similar to new coronal-like morphology and many dense spines provide attachment sites for Ce impregnation (Fig. 1a). With Ce is modified, the spines on spheres of $\text{Mn}_3\text{Ce}_1\text{-MOFs}$ become sparse

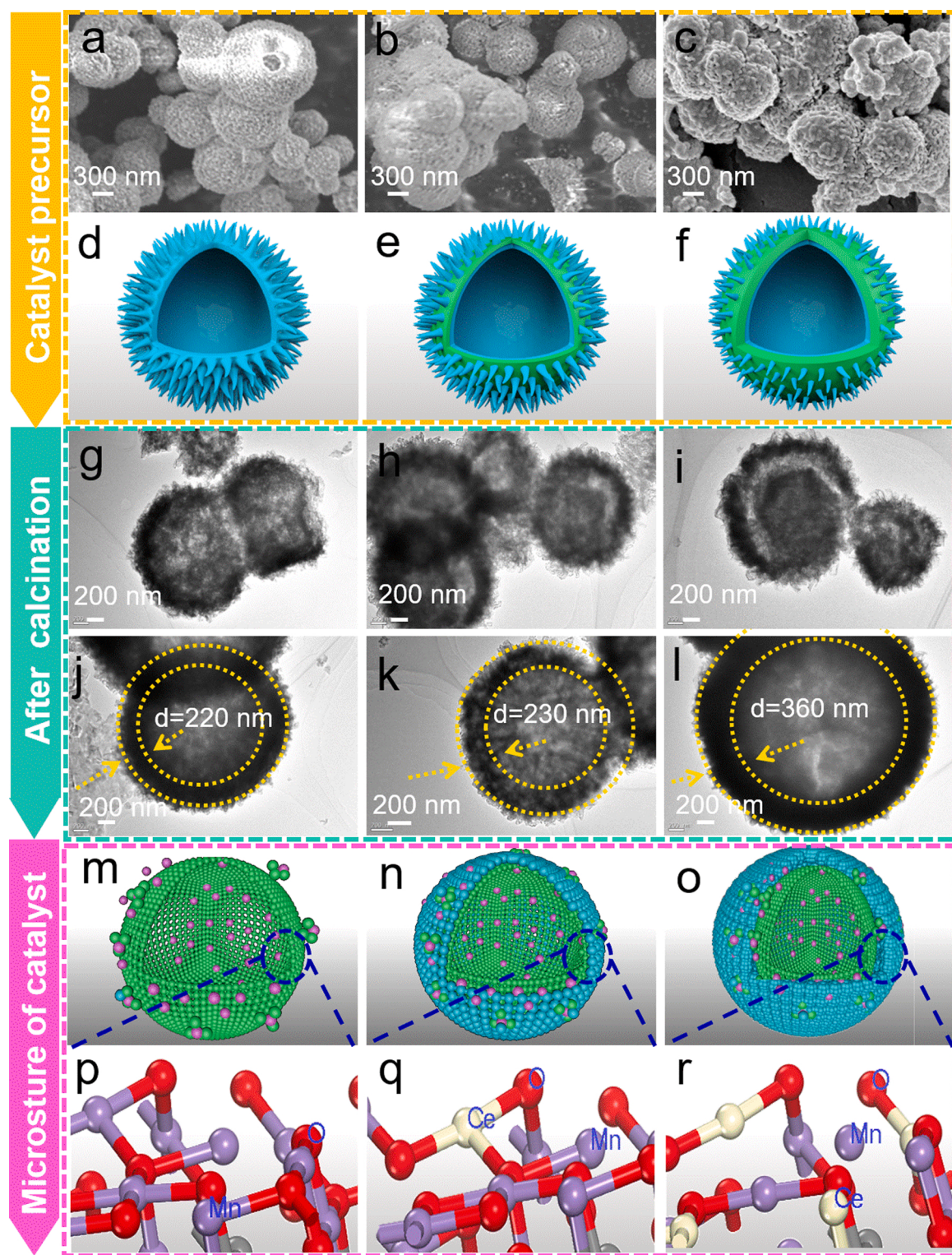


Fig. 1. FESEM images of Mn-MOF (a), Mn₃Ce₁-MOF (b), Mn₂Ce₁-MOF (c), 3D topography of Mn-MOFs (d), Mn₃Ce₁-MOFs (e), and Mn₂Ce₁-MOFs (f); TEM images of MnO_x (g, j), Mn₃Ce₁O_x (h, k), Mn₂Ce₁O_x samples (i, l) and microstructure of MnO_x (m), Mn₃Ce₁O_x (n), and Mn₂Ce₁O_x (o); Structure model of MnO_x (p), Mn₃Ce₁O_x (q) and Mn₂Ce₁O_x (r).

(Fig. 1b). When Ce is further introduced, the spines disappeared slowly, and many small particles are formed to make the surface smooth impregnated on the surface of Mn₂Ce₁-MOFs (Fig. 1c and Fig. S1). The structural diagram of Mn-MOFs, Mn₃Ce₁-MOFs, and Mn₂Ce₁-MOFs are showed in Fig. 1d-f, shows the surface changes of Mn-MOFs, Mn₃Ce₁-MOFs, and Mn₂Ce₁-MOFs, respectively.

To explore the structural characteristics of the catalysts derived from Mn-MOFs, the transmission electrons microscopy (TEM) is performed, as shown in Fig. 1g-l. Since Mn-MOFs and Mn-Ce-MOFs are pyrolyzed during the calcination process, the annealed catalysts of MnO_x and MnCeO_x inherit the microsphere morphology, resulting in a hierarchical hollow structure. The above phenomenon can be explained by the

kirkendall effect [34]. Specifically, the low amplified TEM images display MnO_x sample presented a regular new coronal-like morphology and hollow spheres with a thickness of about 220 nm (Fig. 1g and j). With the introduction of Ce, in Fig. 1h, k, i and l, it is significantly observed that the thicknesses of $\text{Mn}_3\text{Ce}_1\text{O}_x$ and $\text{Mn}_2\text{Ce}_1\text{O}_x$ increase to

230 nm and 360 nm, respectively. Confirming that Ce successfully loaded on the MnO_x concave spherical surface (Fig. S2). Structural diagrams of MnO_x , $\text{Mn}_3\text{Ce}_1\text{O}_x$ and $\text{Mn}_2\text{Ce}_1\text{O}_x$ are shown in Fig. 1m, k and o, respectively. More importantly, Fig. 1p, q and r display the micro-structure characteristics of MnO_x , $\text{Mn}_3\text{Ce}_1\text{O}_x$ and $\text{Mn}_2\text{Ce}_1\text{O}_x$ according to

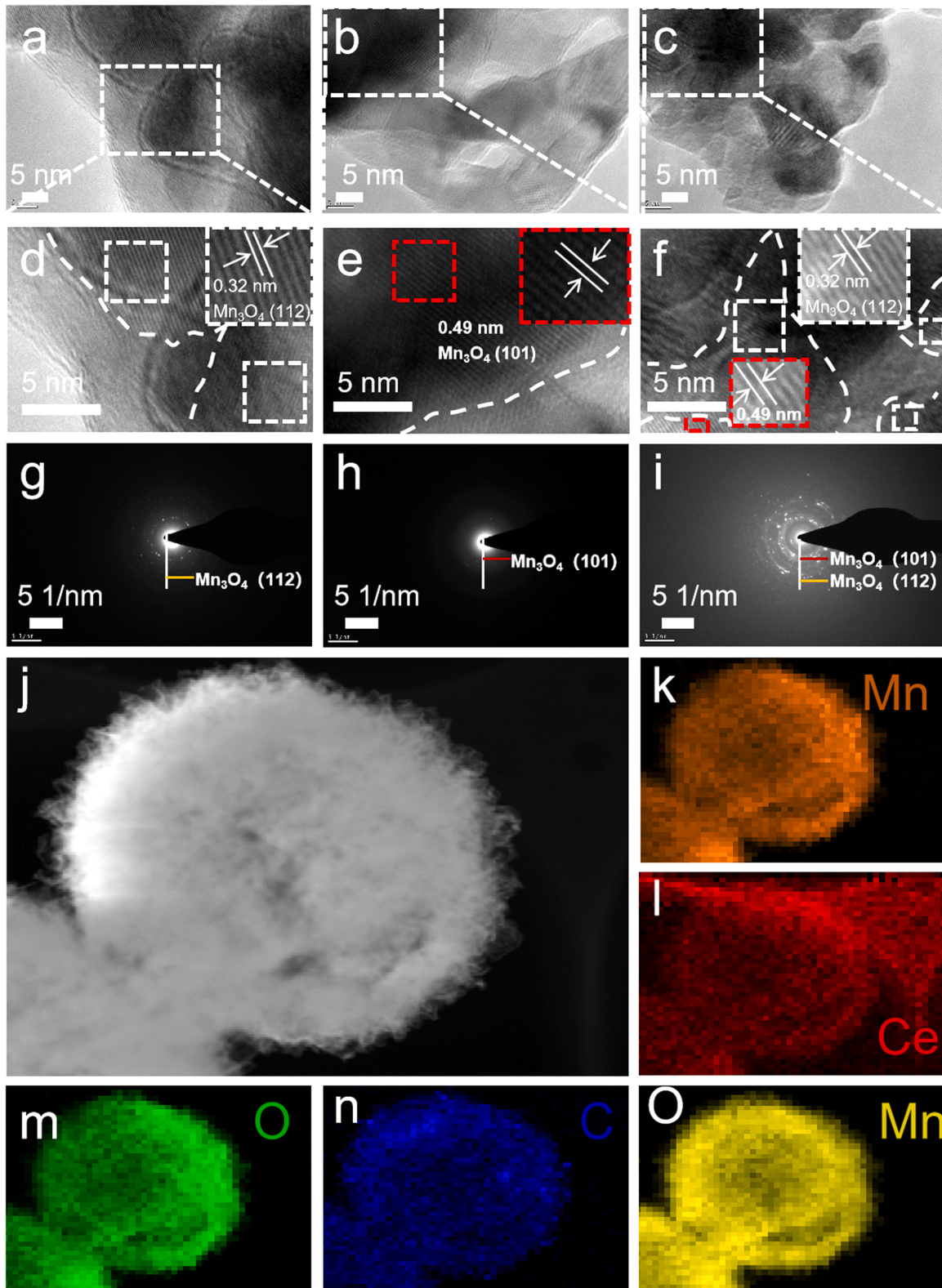


Fig. 2. The TEM images of MnO_x (a, d), $\text{Mn}_3\text{Ce}_1\text{O}_x$ (b, e) and $\text{Mn}_2\text{Ce}_1\text{O}_x$ (c, f); SAED patterns of MnO_x (g), $\text{Mn}_3\text{Ce}_1\text{O}_x$ (h) and $\text{Mn}_2\text{Ce}_1\text{O}_x$ (i); HAADF-STEM images and element mapping images of Mn, Ce, O, and C elements in the $\text{Mn}_2\text{Ce}_1\text{O}_x$ (j-o).

the theoretical calculation results, respectively (see later).

To explore more information about new-coronal like MnCeO_x hollow nanosphere, High-resolution TEM (HRTEM) and selected area electron diffraction (SAED) images of the prepared samples are displayed in Fig. 2. The lattice fringes of pure MnO_x catalyst are distinct and the lattice spacing (0.32 nm) corresponded to (112) plane of Mn_3O_4 , suggesting that the MnO_x catalyst presented high crystallinity (Fig. 2a and d). The lattice fringes of $\text{Mn}_3\text{Ce}_1\text{O}_x$ and $\text{Mn}_2\text{Ce}_1\text{O}_x$ samples are 0.49 and 0.32 nm (Fig. 2b, e, c, and f), which are assigned to the (101) and (112) plane of Mn_3O_4 , respectively. Furthermore, SAED is used to verify specific lattice fringes in Fig. 2g-i. Specifically, the lattice spacing of MnO_x is 0.32 nm (Fig. 2g), and the lattice spacing of $\text{Mn}_3\text{Ce}_1\text{O}_x$ is 0.49 nm (Fig. 2h), while the lattice spacing of $\text{Mn}_2\text{Ce}_1\text{O}_x$ is 0.32 nm and 0.49 nm (Fig. 2i), which are consistent with their lattice images, respectively. Moreover, Mn, Ce, O and C elements mapping of $\text{Mn}_2\text{Ce}_1\text{O}_x$ is shown in Fig. 2j-o. Obviously, the elements are evenly distributed, which indicates that Mn, Ce and O species are well dispersed in MnO_x hollow nanosphere. It is an important factor in o-DCB oxidation reaction.

3.2. Structural characterization of samples

To explore the changes in specific surface area and pore structure after the adjustment of the Ce content as well as new coronal hollow structure, the N_2 adsorption-desorption isotherm and pore size distribution patterns of MnCeO_x catalysts are performed (Fig. 3a). All samples

exhibit the classical type-IV isotherms with an H3 typical hysteresis loop by IUPAC, which indicates that the catalysts possessed a mesoporous structure [33]. Combined with the pore size distribution in Fig. 3b, the most probable pore diameters of MnO_x , $\text{Mn}_3\text{Ce}_1\text{O}_x$ and $\text{Mn}_2\text{Ce}_1\text{O}_x$ are 2–50 nm, demonstrating the mesoporous structure of MnCeO_x catalysts [35]. Furthermore, as displayed in Table 1, the pore size of MnO_x , $\text{Mn}_3\text{Ce}_1\text{O}_x$ and $\text{Mn}_2\text{Ce}_1\text{O}_x$ is 32.62, 14.39, and 15.41 nm. It is worth noting that compared with MnO_x , the pore size of $\text{Mn}_3\text{Ce}_1\text{O}_x$ and $\text{Mn}_2\text{Ce}_1\text{O}_x$ are reduced, suggesting that Ce species successfully enter the mesoporous channels of MnO_x , which provides favorable conditions for the interaction and electron transfer between Mn and Ce species. The specific surface area of MnO_x , $\text{Mn}_3\text{Ce}_1\text{O}_x$ and $\text{Mn}_2\text{Ce}_1\text{O}_x$ are 13.99, 62.06

Table 1

Pore structure information of MnCeO_x catalysts.

Catalysts	Surface area ($\text{m}^2 \text{ g}^{-1}$) ^a	Pore size (nm)	Pore volume ($\text{cm}^3 \text{ g}^{-1}$) ^b	Crystallite size ^c (nm)
MnO_x	13.99	32.62	0.146	11.2
$\text{Mn}_2\text{Ce}_1\text{O}_x$	44.38	15.41	0.186	8.3
$\text{Mn}_3\text{Ce}_1\text{O}_x$	62.06	14.39	0.240	9.1

^a Determined on the desorption branch.

^b Adsorbed volume at $P/P_0 = 0.997$.

^c The crystallite size of Mn_3O_4 (211) is calculated according to the Scherrer equation.

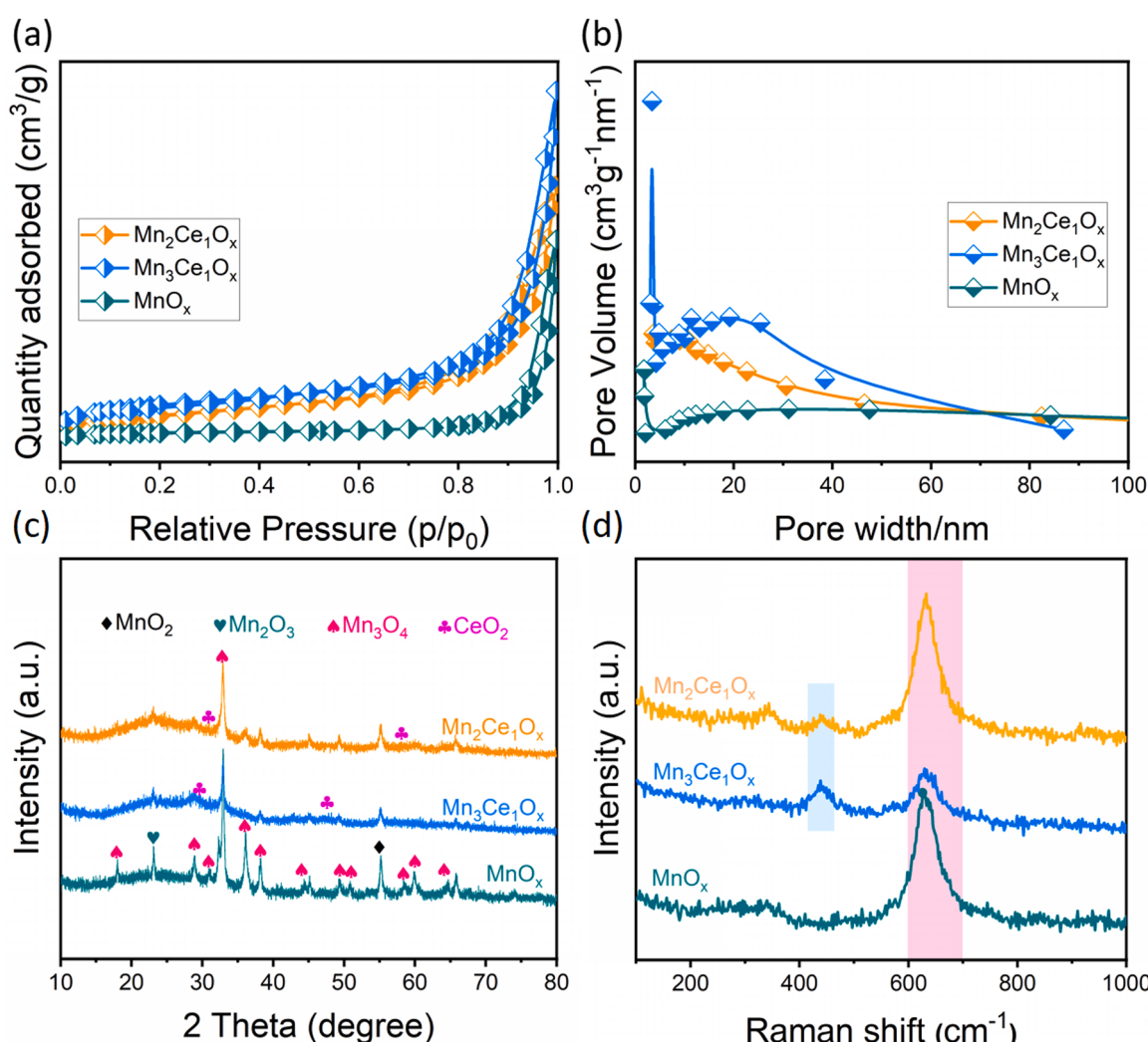


Fig. 3. N_2 adsorption-desorption isotherm (a), Pore size distribution (b), XRD patterns (c) and Raman patterns (d) of MnCeO_x catalysts.

and, $44.38 \text{ m}^2/\text{g}$, respectively. It can be noted that the specific surface area of $\text{Mn}_3\text{Ce}_1\text{O}_x$ and $\text{Mn}_2\text{Ce}_1\text{O}_x$ catalysts is bigger than MnO_x , suggesting that the active component Ce is successfully impregnated on the MnO_x precursor. The introduction of Ce greatly increases the specific surface area of the catalyst, which is conducive to the exposure of more active species on MnCeO_x catalyst. The results show that doping a certain amount of Ce significantly changes the structural characteristics of the material. This can be attributed to the decrease of crystallinity of the catalyst, which is caused by Ce doping. In addition, it is previously reported that the introduction of Ce inhibited the shrinkage of precursors during pyrolysis [36].

To confirm phase composition of all samples, (X-ray diffraction) XRD is displayed in Fig. 3c. The diffraction peaks of all samples are attributed to oxidized species of Mn and Ce. The diffraction peaks at 18.0° (101), 28.9° (112), 31.0° (200), 32.3° (103), 36.1° (211), 38.0° (004), 44.4° (220), 50.7° (105), 53.9° (312), 58.5° (321), 60.0° (224) and 60.4° (400) are correlated to the Mn_3O_4 phase (PDF # 24-0734) [37]. Further, weak diffraction peaks at 28.5° (111), 33.1° (200), 47.5° (220) and 56.3° (311) are correlated to the CeO_2 phase (PDF # 34-0394) in $\text{Mn}_3\text{Ce}_1\text{O}_x$ and $\text{Mn}_2\text{Ce}_1\text{O}_x$, and the weak diffraction peak of CeO_2 indicates that Ce is highly dispersed. It is worth noting that with the

increase of Ce content, the position of the Mn species diffraction peak does not change, but the intensity of the diffraction peak becomes weaker, indicating that some manganese oxide is highly dispersed or existed in amorphous structure, which is conducive to more defect positions in these samples. It is further conducive to more oxygen vacancies. In addition, the average crystal sizes of MnO_x , $\text{Mn}_3\text{Ce}_1\text{O}_x$ and $\text{Mn}_2\text{Ce}_1\text{O}_x$ are calculated by the Scherrer formulation of Mn_3O_4 (211) diffraction peaks and listed in Table 1. It shows that the existence of Ce reduces the crystallinity of MnCeO_x . The grain size of MnO_x decreases with the introduction of Ce. Similar reports have been reported in the previous literature [38]. The introduction of Ce species significantly changed the crystal phase, such as MnO_2 and Mn_2O_3 , which disappear in $\text{Mn}_3\text{Ce}_1\text{O}_x$ and $\text{Mn}_2\text{Ce}_1\text{O}_x$ catalysts. The valence state of MnO_x has an impact on the catalytic oxidation performance of VOCs. In general, the catalytic activity is arranged in the descending order of: $\text{Mn}_3\text{O}_4 > \text{Mn}_2\text{O}_3 > \text{MnO}_2$ [39]. So we speculate that o-DCB also comply this rule. In conclusion, there is a strong interaction between Mn and Ce oxides. To further clarify the structure of the catalyst, all samples are characterized by Raman spectroscopy.

Raman spectroscopy is used to detect potential oxygen vacancies of MnCeO_x catalysts in oxide materials affecting surface reactivity. As

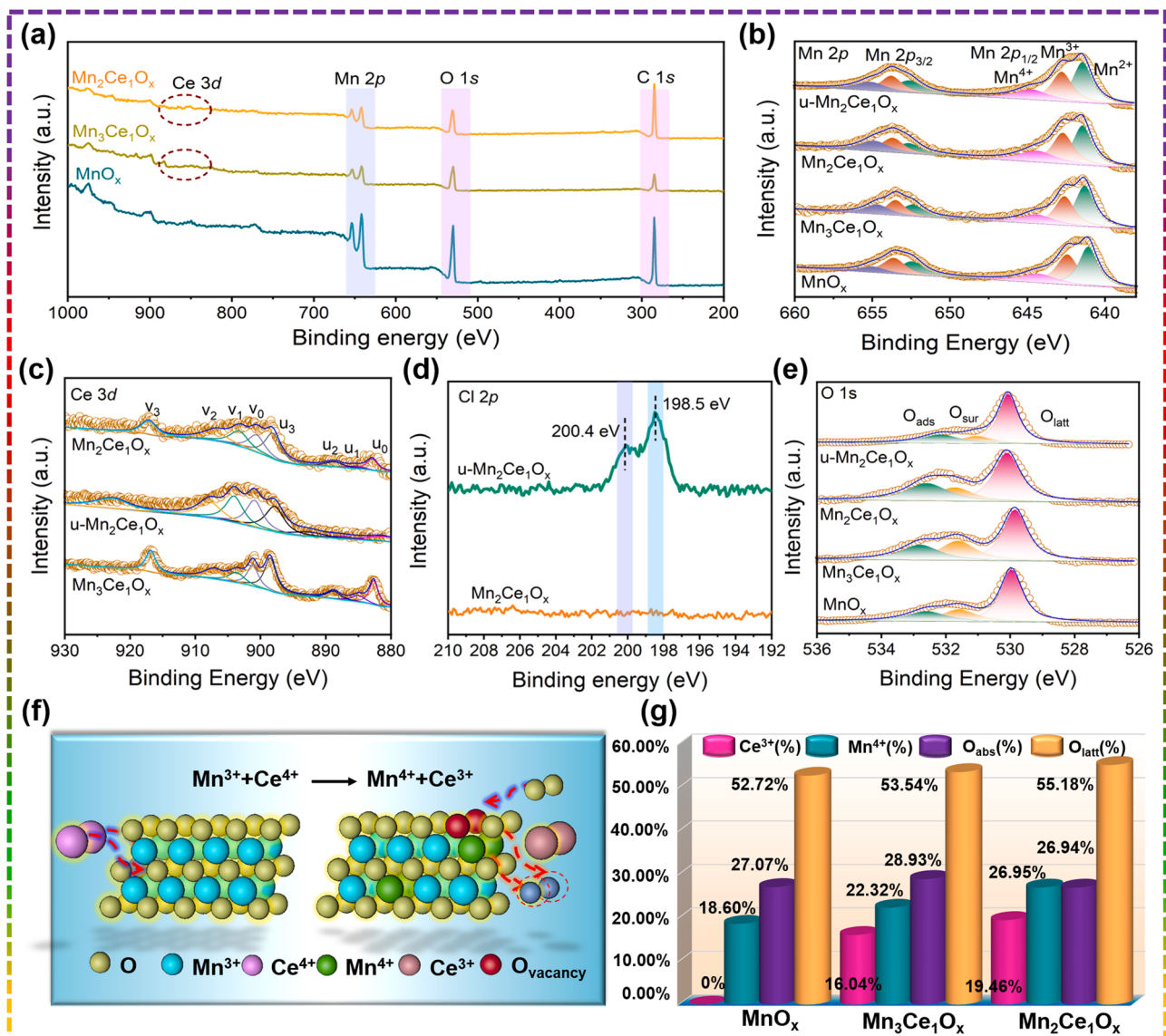


Fig. 4. Survey XPS spectra (a), high resolution XPS of Mn 2p (b), Ce 3d (c), Cl 2p (d), O 1s (e). Interaction of Mn-Ce on surface of MnCeO_x catalysts (f) and the relative proportion of catalysts active species (g).

shown in Fig. 3d, significant bands near 634 cm^{-1} in MnO_x , $\text{Mn}_3\text{Ce}_1\text{O}_x$ and $\text{Mn}_2\text{Ce}_1\text{O}_x$ samples are observed, which are correlated to Mn-O-Mn stretching [40]. Moreover, with the gradual introduction of Ce, the strength of the bands (near 634 cm^{-1}) decreases gradually, indicating that there is a strong interaction between Mn and Ce, which is consistent with the XRD characterization results. Even more interesting is that when Ce species are introduced, the characteristic band of CeO_2 is found at 460 cm^{-1} , assigning to the F_{2g} vibration mode in fluorite cubic structure. It is worth noting that compared with pure MnO_x , there is a significant blueshift in the spectrum related to manganese oxide in MnCeO_x catalysts. With the increase of Ce content, the blue shift is more significant. The blue shift indicates that there are lattice defects in MnCeO_x , which are closely related to the formation of oxygen vacancies [41].

3.3. Surface properties and temperature programmed characterizations of samples

3.3.1. Surface properties

XPS analysis (Mn 2p, Ce 3d, Cl 2p and O1s) of MnCeO_x and u- $\text{Mn}_2\text{Ce}_1\text{O}_x$ after reaction catalysts is conducted to investigate chemical valance of surface elements on catalytic performance in Fig. 4. The Mn 2p XPS spectra of all MnCeO_x catalysts are listed in Fig. 4 and Table 2.

Fig. 4a exhibits the elemental peaks corresponding to Mn, Ce, Cl and O of MnCeO_x . Fig. 4b displays the Mn 2p XPS spectrum of catalysts in a range between 640 and 660 eV. The binding energies at 640.0–650.0 eV and 650.00–660 eV can be attributed to Mn 2p_{3/2} and Mn 2p_{2/1}, respectively [37]. The deconvoluted Mn 2p spectrum for all catalysts assign to three contributions. Mn^{2+} has the lowest binding energy ranging from 640.98 eV to 641.68 eV. The range of 642.06–643.19 eV and 644.64–645.02 eV could be assigned to Mn^{3+} and Mn^{4+} , respectively. These results are consistent with previous literature [42]. Table 2 lists the relative surface formation of manganese with distinct valences states. Obviously, the introduction of Ce has a significant effect on the content of Mn^{4+} species, and the highest $\text{Mn}^{4+}/\text{Mn}_{\text{total}}$ ratio (26.95%) is obtained from $\text{Mn}_2\text{Ce}_1\text{O}_x$, whereas the lowest ratios occur from MnO_x (Table 2), indicating that the content of Mn^{4+} species increases with the gradual increase of Ce content. Furthermore, compared with $\text{Mn}_2\text{Ce}_1\text{O}_x$, the $\text{Mn}^{4+}/\text{Mn}_{\text{total}}$ ratio of u- $\text{Mn}_2\text{Ce}_1\text{O}_x$ is 23.02%, which is lower than that of fresh $\text{Mn}_2\text{Ce}_1\text{O}_x$ sample (Table 2), which shows that Mn^{4+} plays an important role in catalytic oxidation reaction.

The Ce 3d spectrum of MnO_x , $\text{Mn}_3\text{Ce}_1\text{O}_x$ and $\text{Mn}_2\text{Ce}_1\text{O}_x$ catalysts in Fig. 4c can be deconvoluted into eight peaks, where v_1 and u_1 are ascribed to the Ce^{3+} , u_0 , u_2 , u_3 , v_0 , v_2 and v_3 are ascribed to the Ce^{4+} [43–45]. Introducing Ce into Mn-based catalyst can significantly improve the charge transfer rate ($\text{Mn}^{3+} + \text{Ce}^{4+} \rightarrow \text{Mn}^{4+} + \text{Ce}^{3+}$), and the appearance of Ce^{3+} indicates the formation of oxygen vacancy [22,33]. Interestingly, combined with the XPS results of Mn, we find that the ratio of surface Mn^{4+}/Mn and Ce^{3+}/Ce ratio has an excellent linear relationship (Fig. S3). Therefore, the addition of Ce in the MnCeO_x sample may lead to a redox cycle. Therefore, the range of oxygen vacancies in $\text{Mn}_3\text{Ce}_1\text{O}_x$ and $\text{Mn}_2\text{Ce}_1\text{O}_x$ catalysts can be evaluated by the content of Ce^{3+} species. Accordingly, the $\text{Ce}^{3+}/\text{Ce}^{4+}$ ratio of catalysts is listed in Table 2. We found that $\text{Mn}_2\text{Ce}_1\text{O}_x$ contains more Ce^{3+} species, which means that it has more Ce^{3+} and oxygen vacancies. After reaction, the $\text{Ce}^{3+}/\text{Ce}^{4+}$ ratio of u- $\text{Mn}_2\text{Ce}_1\text{O}_x$ sample decreased to 23.17% (Table 2), showing that Ce^{3+} acts as an active component in the reaction.

Table 2
XPS results of MnCeO_x catalysts.

Catalysts	Mn^{4+} (%)	$\text{Mn}^{4+}/\text{Mn}^{3+}$	Ce^{3+} (%)	$\text{Ce}^{3+}/\text{Ce}^{4+}$	O_{latt} (%)	O_{obs} (%)
MnO_x	18.60	0.46	—	—	52.72	27.07
$\text{Mn}_2\text{Ce}_1\text{O}_x$	26.95	0.74	19.46	24.16	55.18	26.94
$\text{Mn}_3\text{Ce}_1\text{O}_x$	22.32	0.63	16.04	19.09	53.54	28.93
u- $\text{Mn}_2\text{Ce}_1\text{O}_x$	23.02	0.64	21.72	23.17	48.32	23.47

The Cl 2p spectrum of $\text{Mn}_2\text{Ce}_1\text{O}_x$ and u- $\text{Mn}_2\text{Ce}_1\text{O}_x$ after reaction samples is shown in Fig. 4d. It should be noted that there are no apparent peaks on the fresh $\text{Mn}_2\text{Ce}_1\text{O}_x$ catalyst. However, two apparent peaks with binding energies of 198.5 and 200.4 eV can be found on the u- $\text{Mn}_2\text{Ce}_1\text{O}_x$ catalyst, which is the characteristics of mineral Cl^- species [20]. This shows that Cl^- species can be deposited on the sample surface during the catalytic combustion of o-DCB, which reduces the catalytic performance or stability of the $\text{Mn}_2\text{Ce}_1\text{O}_x$ catalyst.

The O 1s species have an essential impact on the performance of Mn-based catalysts, so we conduct O 1s analysis in Fig. 4e and Table 2. O 1s spectrum can be fitted into three peaks at 529.3–529.8 eV, 530.0 eV, and 531.7–531.9 eV (Fig. 4e), which belongs to lattice oxygen (O_{latt}), chemical adsorption oxygen species (O_{ads}), and the adsorbed molecular water (O_{sur}), respectively [46,47]. Consequently, the content of O_{ads} and O_{latt} is summarized in Fig. 4g and Table 2. It is observed that the content of O_{latt} is arranged in increasing order: $\text{MnO}_x < \text{Mn}_3\text{Ce}_1\text{O}_x < \text{Mn}_2\text{Ce}_1\text{O}_x$, which means that with the increase of Ce content, the O_{latt} species of catalyst also gradually increases. According to literature reports, the removal of O_{latt} species contributes to oxygen vacancies [33]. In conclusion, $\text{Mn}_2\text{Ce}_1\text{O}_x$ has more oxygen vacancies, which is consistent with the XPS analysis of Ce 3d.

Based on the above characterization results, we explore the interaction of Mn-Ce on the surface of MnCeO_x . As shown in Fig. 4f, when Ce is doped, the content of Mn^{3+} on the surface of $\text{Mn}_2\text{Ce}_1\text{O}_x$ catalyst is reduced. The range of Mn^{4+} is increased, indicated that Ce doping leads to the interaction between Ce^{4+} and Mn^{3+} ($\text{Mn}^{3+} + \text{Ce}^{4+} \rightarrow \text{Mn}^{4+} + \text{Ce}^{3+}$), resulting in more abundant Mn^{4+} and Ce^{3+} on the surface of $\text{Mn}_2\text{Ce}_1\text{O}_x$. The existence of Ce^{3+} leads to an unbalanced chemical state, resulting in the generation of surface oxygen species or oxygen vacancies. At the same time, the generation of oxygen vacancies provides favorable conditions for the adsorption of gaseous oxygen. The above results show that Ce doping can promote the generation of surface reactive oxygen species and induce higher catalytic oxidation performance of o-DCB (see later) [22,38].

3.3.2. Temperature programmed characterizations

Temperature programmed reduction of H_2 ($\text{H}_2\text{-TPR}$) is performed to investigate the redox properties of MnCeO_x catalysts. For ease understanding, the $\text{H}_2\text{-TPR}$ curves of MnO_x , $\text{Mn}_2\text{Ce}_1\text{O}_x$ and $\text{Mn}_3\text{Ce}_1\text{O}_x$ catalysts are fitted and marked as α , β and γ . The α peak can be recorded as the reduction of MnO_2 to Mn_3O_4 , and the β and γ peaks are noted as the reduction of Mn_3O_4 to MnO [48]. As shown in Fig. 5a and Table S1, the reduction peaks positions of the catalysts are in the following order: $\text{MnO}_x > \text{Mn}_3\text{Ce}_1\text{O}_x > \text{Mn}_2\text{Ce}_1\text{O}_x$, which indicates that the low-temperature reducibility of $\text{Mn}_2\text{Ce}_1\text{O}_x$ is the best and that of pure MnO_x is the worst. It is worth noting that with the introduction of Ce, the reduction peak of the catalysts gradually moves to the low temperature region. It further shown that the interaction between manganese oxide and cerium oxide can improve the mobility of oxygen species by forming solid solutions to promote the reduction of manganese species [49]. High low-temperature reducibility is conducive to the transfer of oxygen from the bulk to the surface, which further enables the catalytic efficiency in the catalytic oxidation reaction. Therefore, perfect low-temperature reducibility usually shows excellent catalytic oxidation activity.

To identify and quantify the surface oxygen species, Fig. 5b presents the $\text{O}_2\text{-TPD}$ plots of all catalysts with different Ce contents. Three types

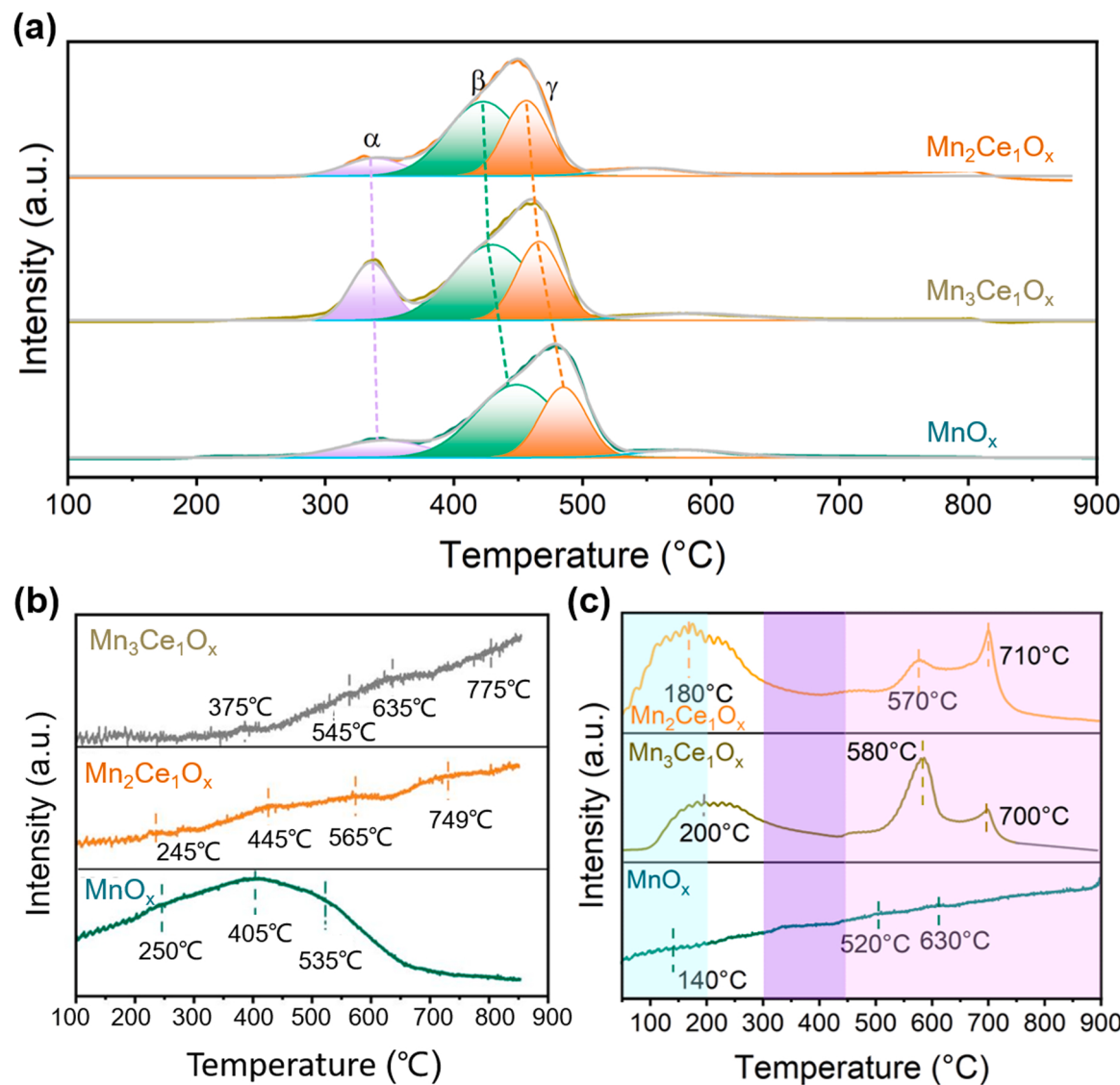


Fig. 5. H₂-TPR profiles (a), O₂-TPD curve (b), NH₃-TPD diagram (c) of MnCeO_x catalysts.

of O₂ desorbed peaks are found in three samples, suggesting three various forms of oxygen species on the catalyst surface [50]. The broad peak in low-temperature (245–375 °C) can belong to the desorption of chemical adsorbed oxygen species. The peak of 405–565 °C could be ascribed to the desorption of surface adsorbed oxygen species. The peak centered between 635 and 775 °C is characteristic of surface lattice oxygen [51]. It is worth noting that, compared with pure MnO_x, the peak in 245–375 °C decreased and the peak in 405–775 °C increased substantially when Ce is doped, indicating that the introduction of Ce reduces the surface adsorbed oxygen and significantly improves the species of chemically adsorbed oxygen and lattice oxygen. This may be due to the following reasons. Firstly, Ce species enter the lattice of MnO_x, resulting in lattice defects in MnCeO_x and richer oxygen vacancies. Secondly, the interaction forms between Mn and Ce with the introduction of Ce. When the doping ratio of Mn/Ce was 2:1, the peak corresponding to lattice oxygen was broader and more robust, which indicates that Mn₂Ce₁O_x contains more lattice oxygen species, which is consistent with the XPS characterization of O 1 s. In addition, compared with pure MnO_x catalyst, the peaks of Mn₃Ce₁O_x and Mn₂Ce₁O_x shift to higher temperatures, suggesting that Ce can improve the thermal stability of the Mn-based catalysts (see later).

The acid characteristics of MnCeO_x samples with different Ce content

are determined by NH₃-TPD and the results are exhibited in Fig. 5c. The peaks in the light blue shadow are attributed to the NH₃ desorption at the weak acid sites, and the peaks in the white, purple and pink regions belong to the NH₃ desorption at moderate, strong and super-strong acids, respectively [35]. It should be noted that after doping Ce in the samples, the desorption peaks of Mn₃Ce₁O_x and Mn₂Ce₁O_x appear in the blue and pink regions interpreted as a weak acid and super-strong sites, respectively, which indicates that Ce can significantly improve the acidity of the catalysts. In addition, compared with Mn₃Ce₁O_x, Mn₂Ce₁O_x has a broader desorption peak and higher desorption intensity. The result above indicates that the doping of more Ce is beneficial to the increase of acid sites. Previous literature reported that acid sites play an essential role in the catalytic combustion of o-DCB [7,17, 20].

3.4. DFT-calculation study

The density functional theory (DFT) calculation of o-DCB adsorption on Mn₃O₄ (112) surface reveals the effects of Ce doping and oxygen vacancy on the o-DCB catalytic combustion. The theoretical calculation method is listed in the supporting information.

Firstly, the model of o-DCB molecular is optimized as shown in

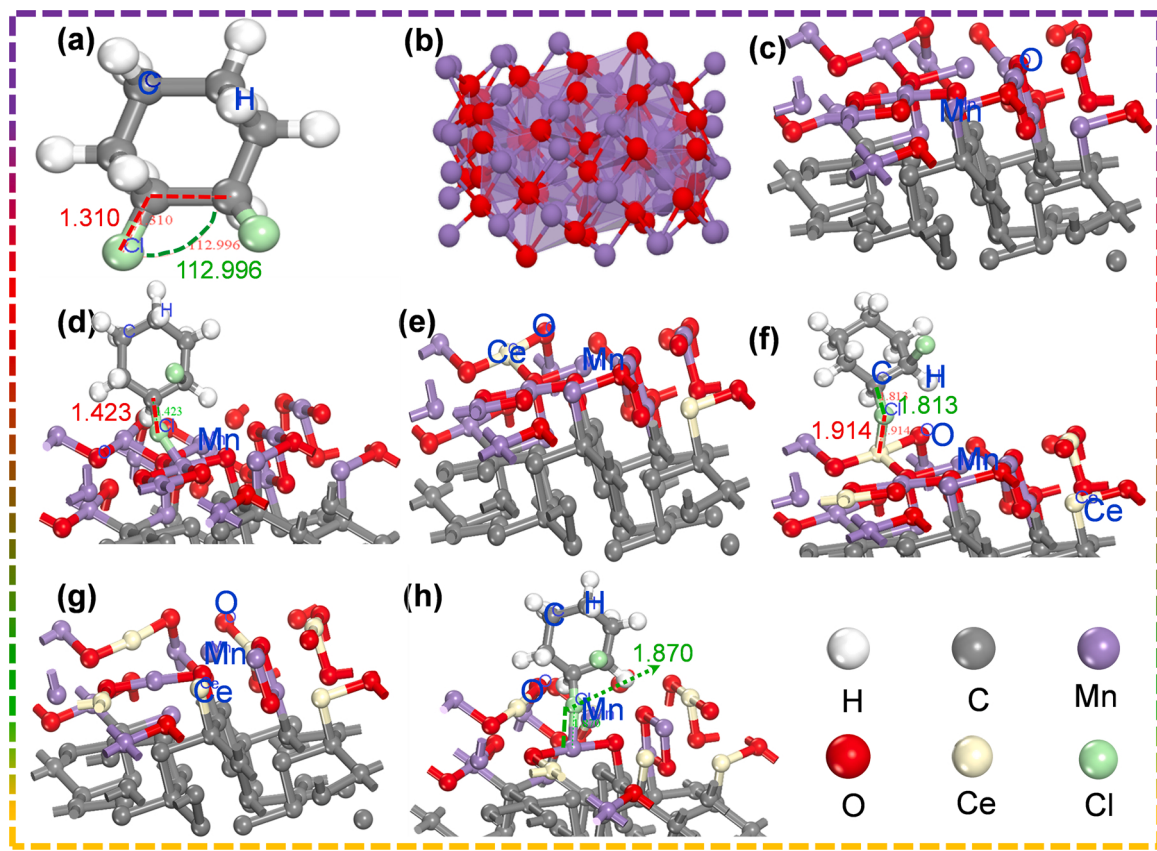


Fig. 6. The optimized model for o-DCB (a), Mn₃O₄ (b), Mn₃O₄ (112) (c), o-DCB adsorbed on Mn₃O₄ (112) (d), Ce-doped Mn₃O₄ (112) (e), o-DCB adsorbed on Ce-doped Mn₃O₄ (112) (f), Oxygen vacancy of Ce-doped Mn₃O₄ (112) (g) and oxygen vacancy of o-DCB adsorbed on Ce-doped Mn₃O₄ (112) (h).

Fig. 6a. Tetragonal Mn₃O₄ is selected with a, b and c are 3.070 Å, 9.725 Å and 9.953 Å respectively, which formation energy and bandgap are – 2.012 and 0 eV (Fig. 6b). The surface of Mn₃O₄ (112) system not only has low surface energy, but also is easier to be exposed under typical adsorption reaction conditions. When Ce is doped in Mn₃O₄ system, Ce atom provides an active site for o-DCB, and the increase of oxygen vacancies is conducive to the adsorption and activation of o-DCB, showing better catalytic performance. In this study, taking Mn₃O₄ system as the substrate, the section of p (4 × 4) Mn₃O₄ (112) is constructed with 83 atoms, and the cell sizes with a, b and c are 10.198 Å, 11.695 Å and 17.276 Å respectively to explore the adsorption of o-DCB on Mn₃O₄ (112) system (Fig. 6c and d). The surface of Mn₃O₄ (112) is doped with Ce to construct different oxygen vacancies to study the effect of oxygen vacancy on the adsorption of o-DCB on Mn₃O₄ (112) surface doped Ce system (Fig. 6g and h).

In the theoretical calculation of adsorption energy, the atoms in the bottom two atomic layers are fixed at their initial positions in the equilibrium structure, and the top two atomic layers and adsorbents are released. The system reaches a stable state through geometric optimization. The adsorption energy (E_{ads}) of C₆H₁₂Cl₂ adsorbed on the surface of Mn₃O₄ (112) is defined as [52]:

$$E_{\text{ads}} = E_{\text{TG}} + E_{\text{o-DCB}} - E_{\text{Total}}$$

Where: E_{TG} is the total energy of Mn₃O₄ (112) system, and E_{o-DCB} is the energy of a single o-DCB molecule, E_{Total} is the total energy of adsorbing a o-DCB molecule on Mn₃O₄ (112) system.

The o-DCB model is optimized to obtain the molecular configuration of o-DCB with C-Cl bond length of 1.760 Å and C-C-Cl bond angle of 109.453°, and the model tends to be the most stable state for the system. As shown in Fig. 7a, the most stable state of o-DCB molecule adsorbed on Ce-doped Mn₃O₄ (112) models is obtained after geometric optimization.

Additionally, the adsorption of o-DCB on the catalysts with 2, 4, 6, 8 and 10 Ce atoms doped Mn₃O₄ is calculated and their structure is optimized to obtain a stable adsorption model. The six adsorption configurations are represented by o-DCB-Ce₀, o-DCB-Ce₂, o-DCB-Ce₄, o-DCB-Ce₆, o-DCB-Ce₈ and o-DCB-Ce₁₀, respectively as shown in Fig. 7b-g. Through simulation calculation, the optimized o-DCB molecule is adsorbed on the surface of Mn₃O₄ (112) doped with 6 Ce atoms. It is found that the bond length of C-Cl changed significantly from 1.760 Å to 4.273 Å, and that of Ce-Cl from 1.914 Å to 4.799 Å, confirming that o-DCB molecule is adsorbed on the surface of Mn₃O₄ (112) doped with 6 Ce atoms. C-C-Ce bond angle of o-DCB-Ce₆ is 115.039°. o-DCB molecule is activated in a six Ce atoms doped Mn₃O₄ (112) model to produce chemical adsorption.

Through the calculation of o-DCB molecule adsorbed on the surface of Mn₃O₄ (112) doped with different Ce atoms, a good adsorption effect is obtained with o-DCB adsorbed on 6 Ce atoms doped Mn₃O₄ (112). In exploring the adsorption of o-DCB molecule at the oxygen defect position on the surface of Ce doped Mn₃O₄ (112), the Mn₃O₄ (112) system doped with 6 Ce atoms is geometrically optimized in the calculation. Three adsorption configurations are represented by o-DCB-VO₄, o-DCB-VO₈ and o-DCB-VO₁₂ in Fig. 7h-j. Through simulation calculation, the optimized molecular geometry is o-DCB adsorbed on the (112) plane of o-DCB-Ce₆ catalyst with four oxygen vacancy. It is found that the C-Cl bond length changes significantly, from 1.760 Å to 5.602 Å, and the Ce-Cl bond changes from 1.914 Å to 5.164 Å, indicating that o-DCB molecule is adsorbed on the o-DCB-VO₄ in Fig. 7h. The C-C-Ce bond angle is 86.529°, and o-DCB molecule is activated on four oxygen vacancy systems of Mn₃O₄ (112) doped with 6 Ce atoms to produce chemisorption.

It is observed that the introduction of appropriate Ce atoms will improve the adsorption effect of Mn₃O₄ (112) on o-DCB. By comparing the adsorption effects of o-DCB on Mn₃O₄ (112) systems doped with different Ce atom, we observe that the Mn₃O₄ (112) system doped with 6 Ce atoms (o-DCB-Ce₆) exhibit good adsorption properties of o-DCB, and

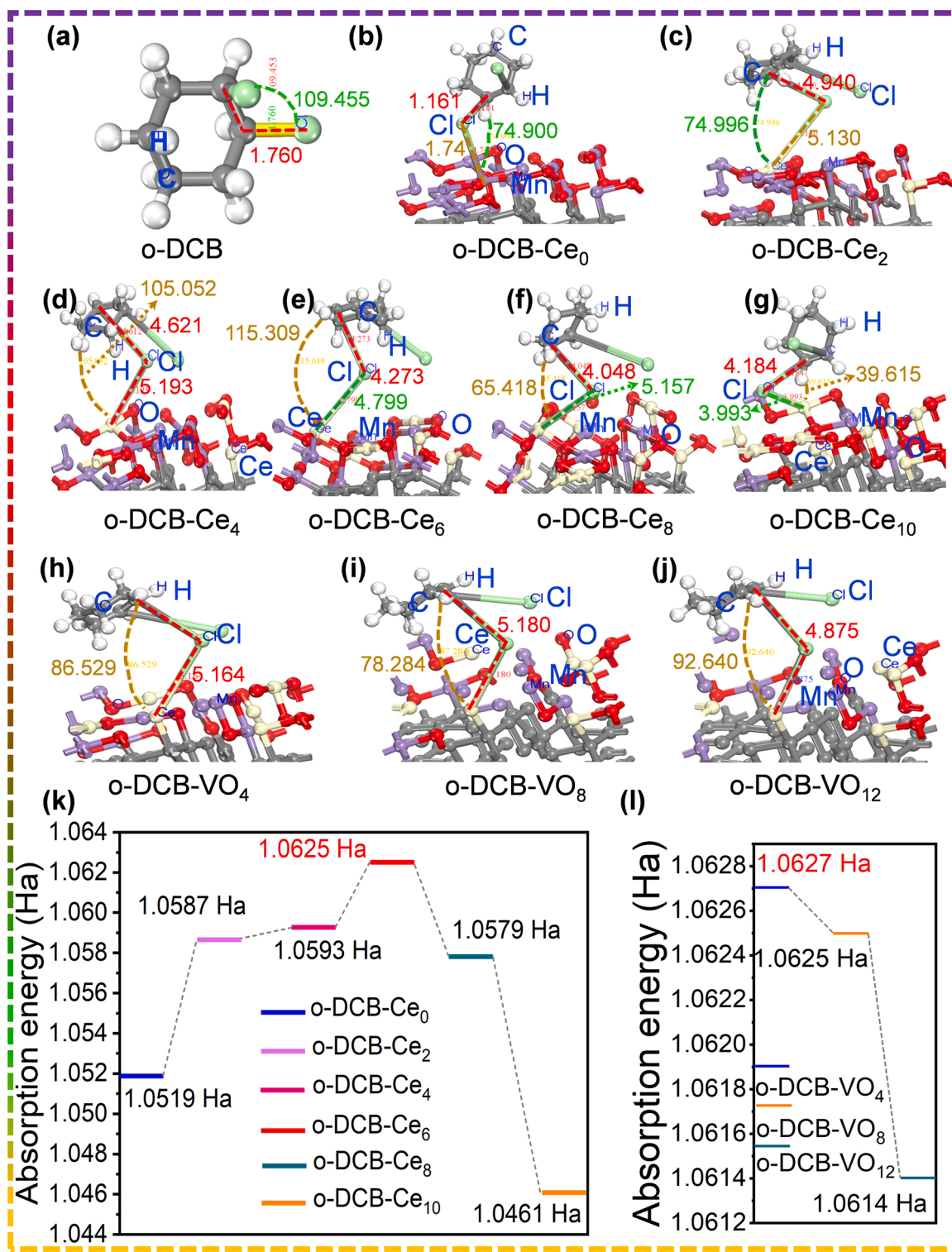


Fig. 7. The optimized model for o-DCB (a), o-DCB-Ce₀ (b), o-DCB-Ce₂ (c), o-DCB-Ce₄ (d), o-DCB-Ce₆ (e), o-DCB-Ce₈ (f), o-DCB-Ce₁₀ (g), o-DCB-VO₄ (h), o-DCB-VO₈ (i), o-DCB-VO₁₂ (j), The energy of o-DCB adsorbed on Mn₃O₄(112) (k) system with different Ce atom and system energies of different oxygen vacancies in Mn₃O₄(112) system doped with 6 Ce atoms (l).

its adsorption energy is 1.0625 Ha. It is worth noting that the adsorption energy will decrease with the increase of Ce atom, which may be due to the increase of Ce atom destroying the Mn₃O₄ (112) system (Fig. 7k and Table 3). Oxygen vacancies contribute to the adsorption and activation of o-DCB and further promote the catalytic performance of the catalyst. The adsorption of o-DCB by different oxygen vacancies in the system is studied as shown in Fig. 7l and Table 3. Obviously, when the number of

oxygen vacancies is 4, the Mn₃O₄ (112) system doped with 6 Ce atoms shows good adsorption performance for o-DCB, and its adsorption energy is 1.0627 Ha.

In summary, the adsorption properties of the Mn₃O₄ (112) doped Ce system for o-DCB are simulated by using the generalized gradient approximation (GGA) and (PBE) pseudopotential of density functional theory. The adsorption energy data of different Ce atom doping and

Table 3

The energy of o-DCB adsorbed on Mn_3O_4 (112) system with different Ce atom and system energies of different oxygen vacancies in Mn_3O_4 (112) system doped with 6 Ce atoms.

System model	E_k/Ha	E_{cor}/Ha	E_{elc}/Ha	E_{TG}/Ha	$E_{\text{o-DCB}}/\text{Ha}$	$E_{\text{Total}}/\text{Ha}$	E_{SA}/Ha	E_{ads}/Ha
o-DCB-Ce ₀	-21.590	7.772	-40.381	-44991.469	-1154.476	-46146.997	-46103.848	1.0519
o-DCB-Ce ₂	10.395	8.426	-72.722	-54679.686	-1154.476	-60984.290	-54734.233	1.0587
o-DCB-Ce ₄	44.022	8.978	-106.709	-53883.260	-1154.476	-75821.373	-53938.341	1.0593
o-DCB-Ce ₆	77.856	9.497	-141.037	-53086.828	-1154.476	-90658.623	-53142.450	1.0625
o-DCB-Ce ₈	109.477	10.043	-173.206	-52290.391	-1154.476	-105495.901	-52346.559	1.0579
o-DCB-Ce ₁₀	142.737	10.607	-206.783	-119179.506	-1154.476	-120335.029	-120288.594	1.0461
o-DCB-VO ₄	80.119	8.950	-141.661	-89202.213	-1154.476	-90357.751	-90314.726	1.0627
o-DCB-VO ₈	81.887	8.492	-141.761	-88901.222	-1154.476	-90056.761	-90014.722	1.0625
o-DCB-VO ₁₂	84.187	8.013	-142.454	-88600.315	-1154.476	-89755.852	-48396.338	1.0614
o-DCB	-2.873	1.023	-1.763	-	-1154.476	-	-1151.675	-

* E_k : Kinetic, E_{cor} : Exchange-correlation, E_{elc} : Electrostatic, E_{TG} : Total energy of doped Mn_3O_4 (112) system, $E_{\text{o-DCB}}$: The energy of a single o-DCB molecule, E_{Total} : The total energy of the o-DCB absorbed system, E_{SA} : Sum of atomic energies, E_{ads} : Absorption energy.

different oxygen vacancies on Mn_3O_4 (112) surface are investigated and analyzed, and doped with 6 Ce atoms has the most considerable adsorption energy and the best adsorption effect for o-DCB with an adsorption energy of 1.0625 Ha. At the same time, the adsorption of o-DCB is simulated in different oxygen vacancies of o-DCB-Ce₆. The 6 Ce atoms doped Mn_3O_4 (112) with four oxygen vacancies showed excellent adsorption performance, and its adsorption energy is as high as 1.0627 Ha. These theoretical calculation results show that Mn_3O_4 (112) system doped with an appropriate amount of Ce and oxygen vacancy is conducive to the catalytic oxidation of o-DCB, and plays a vital role in the adsorption and activation of o-DCB, which can be effectively promoted catalytic oxidation performance of MnCeO_x catalyst.

3.5. Catalytic oxidation of o-DCB over MnCeO_x catalysts

3.5.1. Performance study

The catalytic activity of MnCeO_x catalysts is evaluated for catalytic oxidation of o-DCB under dry air and 5.0 vol% H_2O conditions, respectively. Fig. 8a shows the activity of these catalysts in dry condition. Interestingly, the $\text{Mn}_2\text{Ce}_1\text{O}_x$ hollow nanosphere with $\text{GHSV} = 15000 \text{ mL g}^{-1} \text{ h}^{-1}$ shows the best destructive performance of o-DCB with T_{90} at 335 °C, whereas the $\text{Mn}_3\text{Ce}_1\text{O}_x$ catalyst obtain a conversion of 90% at 350 °C. Notably, the T_{90} of MnO_x catalyst is 385 °C. The above results mean that MnO_x hollow nanosphere owns the insufficient performance for o-DCB catalytic oxidation, and the doping of Ce species significantly improves its performance for o-DCB oxidation, which is due to the strong interaction between Mn-Ce and the introduction of Ce element can effectively improve the adsorption and activation of o-DCB molecules on Mn_3O_4 , as demonstrated by XPS and GGA of DFT (Figs. 4e, 6 and 7). The outstanding catalytic activity of $\text{Mn}_2\text{Ce}_1\text{O}_x$ are mainly attributed to the high reducibility and abundant active species and acid sites as confirmed by $\text{H}_2\text{-TPR}$, $\text{O}_2\text{-TPD}$, XPS and $\text{NH}_3\text{-TPD}$ (Table 1, Figs. 4 and 5). For $\text{Mn}_2\text{Ce}_1\text{O}_x$ catalyst, good catalytic performance is also attributed to its high specific surface area, as demonstrated by BET (Table 1). There is a discernible decline in conversion of o-DCB over MnO_x , $\text{Mn}_2\text{Ce}_1\text{O}_x$ and $\text{Mn}_3\text{Ce}_1\text{O}_x$ catalysts under 5.0 vol% H_2O conditions exhibited in Fig. 8b. This is mainly due to the competitive adsorption between o-DCB and H_2O molecules, resulting in the reduction of catalytic activity of these catalysts.

The cyclicity test over $\text{Mn}_2\text{Ce}_1\text{O}_x$ catalyst under dry air conditions is displayed in Fig. 8c. The T_{90} of $\text{Mn}_2\text{Ce}_1\text{O}_x$ in cycle 1 is 335 °C, and there is no significant decrease in cycles 2 and 3. However, in cycle 4, it rises to 345 °C. It is noteworthy that there is a similar trend under the 5.0 vol% H_2O conditions (Fig. 8d). The T_{50} and T_{90} of $\text{Mn}_2\text{Ce}_1\text{O}_x$ in cycle 1 is 310 and 365 °C, respectively. However, in cycle 4, it rises to 340 and 375 °C, respectively. This is mainly due to the deposition of Cl^- on the surface of $\text{Mn}_2\text{Ce}_1\text{O}_x$ catalyst. Some active sites of $\text{Mn}_2\text{Ce}_1\text{O}_x$ are occupied by Cl^- in the reaction, which results in reduced catalytic performance. In summary, $\text{Mn}_2\text{Ce}_1\text{O}_x$ shows good repeatability and practicality under dry air

and 5.0 vol% H_2O conditions. This is of great significance for industrial applications.

Fig. 8e and f display the selectivity of the $\text{Mn}_2\text{Ce}_1\text{O}_x$ catalyst for o-DCB catalytic oxidation by-products. By analyzing $\text{Mn}_2\text{Ce}_1\text{O}_x$ reaction products, it is found that HCl and CO_2 are the primary products in the whole reaction process. When the reaction temperature is above 200 °C, a small amount of CB and Cl_2 is observed. The yield of Cl_2 is significantly accelerated with the increase of temperature when the reaction temperature is around 326 °C, and no CO is detected in the flowing gas (Fig. 8e). Interestingly, there is a similar trend under 5.0 vol% conditions, as shown in Fig. 8f. It is particularly emphasized that CO_2 selectivity begins to decline at 200 °C under dry conditions (Fig. 8g), while it begins to decline at 220 °C under water conditions (Fig. 8h).

What's more, the water resistance is essential for industrial applications. To further test the comprehensive properties of the prepared materials, Fig. 8i describes the H_2O resistance test with 5.0 vol% H_2O for the MnO_x and $\text{Mn}_2\text{Ce}_1\text{O}_x$. The catalytic performance of the MnO_x catalyst decreases from 70% to 60% at 375 °C, while that of $\text{Mn}_2\text{Ce}_1\text{O}_x$ decreases from 80% to 62% at 325 °C after adding 5.0 vol% H_2O . Interestingly, the performance of the catalysts gradually recovered when the water is removed. This illustrates that the performance of MnO_x decreases more significantly than that of $\text{Mn}_2\text{Ce}_1\text{O}_x$ under wet conditions, indicating that the addition of Ce can also improve the water resistance in the reaction process. In addition, $\text{Mn}_2\text{Ce}_1\text{O}_x$ shows good long-term stability at low temperature (Fig. S7).

The catalytic oxidation activity of o-DCB over $\text{Mn}_2\text{Ce}_1\text{O}_x$ is compared with the literature reported (Fig. 8j and Table S2) [7,15,17,33,46,53–60]. The T_{90} and T_{50} exhibit the lowest temperature, which shows that $\text{Mn}_2\text{Ce}_1\text{O}_x$ has better catalytic performance than congeneric Co_1Mn_1 , $\text{CoMn500} @ 0.5\text{Ti}$, MnCeFe catalyst under dry air conditions. In addition, the synthesis process of $\text{Mn}_2\text{Ce}_1\text{O}_x$ is simple, efficient and energy-saving, and it is an environment-friendly catalyst. More importantly, $\text{Mn}_2\text{Ce}_1\text{O}_x$ has better catalytic performance under 5.0 vol% H_2O conditions than most of the catalysts under dry air conditions, indicating $\text{Mn}_2\text{Ce}_1\text{O}_x$ hollow nanosphere more in line with environmental conditions, and more practical.

3.5.2. Kinetic study

The reaction of o-DCB catalytic oxidation over MnCeO_x hollow nanosphere is controlled within the dynamic region (o-DCB conversion < 25%). The apparent activation energy (E_a) values of MnCeO_x catalyst are calculated by the Arrhenius equation as in previous reports [7,46]. The Arrhenius curves of all catalysts under dry air and 5.0 vol% H_2O conditions are displayed in Fig. 9a and b, respectively. The good linear relationship is gained by fitting the function between $\ln r$ and $1/T$, and E_a values of all catalysts are summarized in Table 4. The E_a values of these catalysts under dry air conditions is 33.41, 29.99 and 27.76 kJ/mol for MnO_x , $\text{Mn}_3\text{Ce}_1\text{O}_x$, and $\text{Mn}_2\text{Ce}_1\text{O}_x$, respectively. While the E_a values under 5.0 vol% H_2O conditions is 41.21, 40.51 and 32.30 kJ/mol for

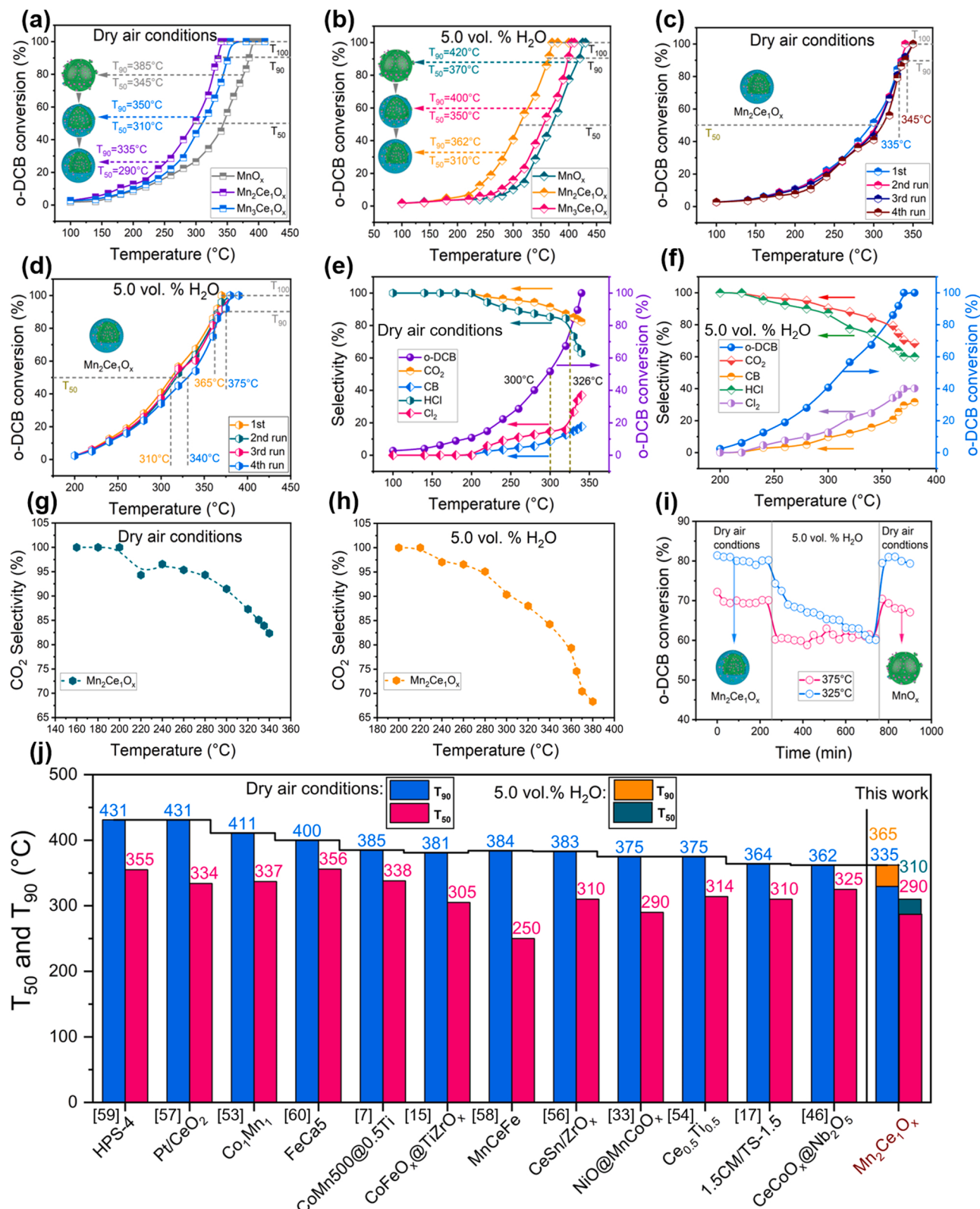


Fig. 8. Catalytic activity of MnCeO_x catalysts: o-DCB conversion curves under dry air conditions (a) and 5.0 vol% H_2O conditions (b), Cycle stability test of $\text{Mn}_2\text{Ce}_1\text{O}_x$ under dry air (c) and 5.0 vol% H_2O conditions (d), chlorination products selectivity of $\text{Mn}_2\text{Ce}_1\text{O}_x$ under dry air (e) and 5.0 vol% H_2O conditions (f), CO_2 selectivity under dry air (g) and 5.0 vol% H_2O conditions (h), hydrothermal stability the MnO_x and $\text{Mn}_2\text{Ce}_1\text{O}_x$ catalysts (i), performance comparison between $\text{Mn}_2\text{Ce}_1\text{O}_x$ catalyst and other reported catalysts in literature (j); Reaction conditions: 1000 ppm o-DCB, 20% O_2 , N_2 balance, GHSV = 15000 $\text{mL g}^{-1} \text{h}^{-1}$, 5.0 vol % H_2O .

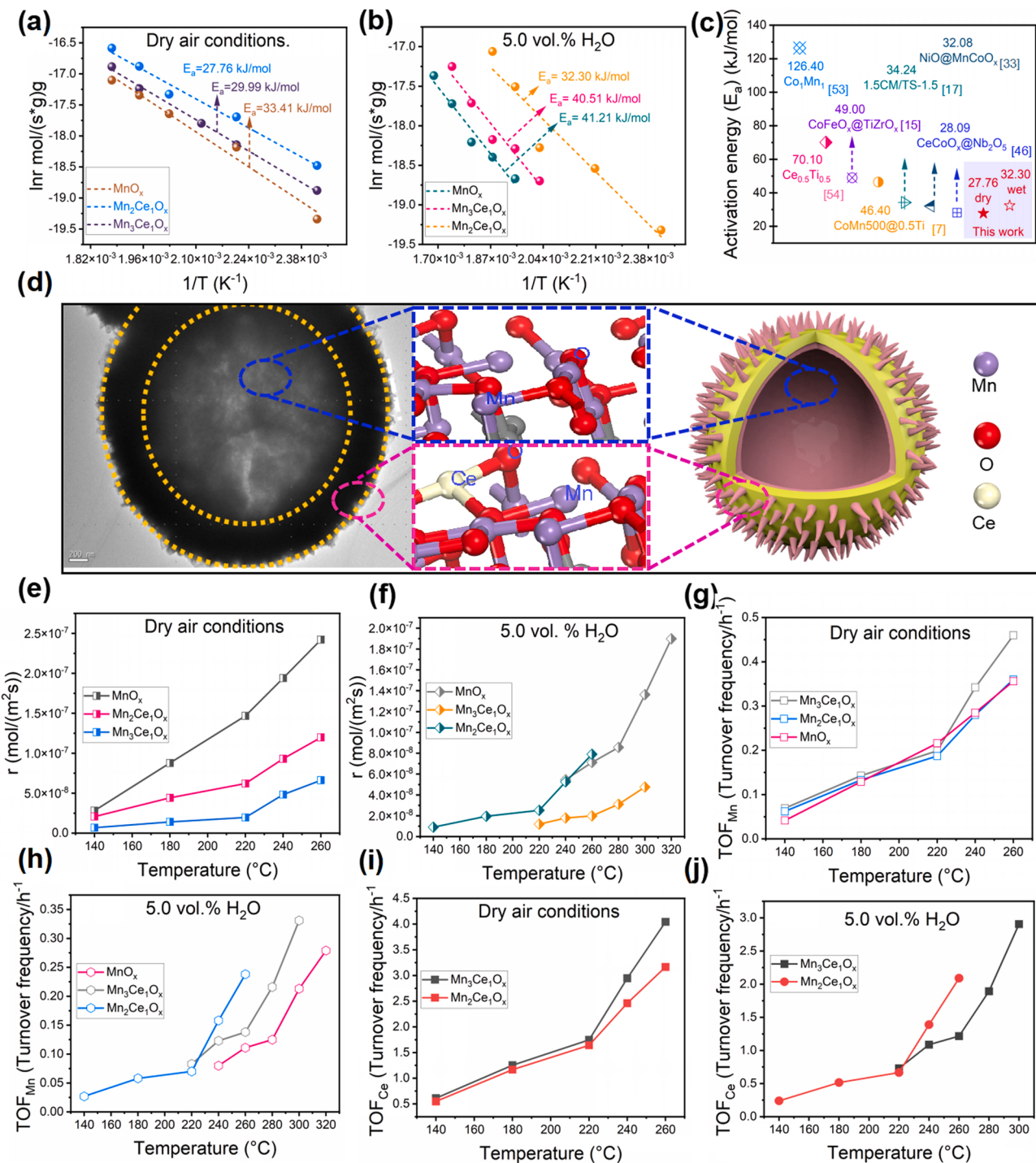


Fig. 9. Arrhenius curves for o-DCB oxidation under dry air (a) and 5.0 vol% H_2O conditions (b), Activation energy of catalysts between $\text{Mn}_2\text{Ce}_1\text{O}_x$ catalyst and that of other reported catalysts (c), Structural characteristics of $\text{Mn}_2\text{Ce}_1\text{O}_x$ hollow nanosphere (d), Reaction rates of catalysts for o-DCB oxidation reaction: under dry air (e) and 5.0 vol% H_2O conditions (f), TOF_{Mn} (g) and TOF_{Ce} (i) value under dry air, and TOF_{Mn} (h) and TOF_{Ce} (j) value under 5.0 vol% H_2O conditions.

MnO_x , $\text{Mn}_3\text{Ce}_1\text{O}_x$, and $\text{Mn}_2\text{Ce}_1\text{O}_x$, respectively. Obviously, $\text{Mn}_2\text{Ce}_1\text{O}_x$ hollow nanosphere with the smallest E_a under dry air and 5.0 vol% H_2O conditions, which shows that $\text{Mn}_2\text{Ce}_1\text{O}_x$ has a best ability to destroy o-DCB in kinetics, consistent with the performance test results (Fig. 8a and b). The E_a value of $\text{Mn}_2\text{Ce}_1\text{O}_x$ is the lowest compared with that reported in the literature (Fig. 9c), which means that $\text{Mn}_2\text{Ce}_1\text{O}_x$ has better kinetic ability to destroy o-DCB compared with other catalysts [7,15,17, 33,46,53,54]. Further, the reason for the lowest E_a value of $\text{Mn}_2\text{Ce}_1\text{O}_x$ is related to its unique microstructure (Fig. 9d). Specifically, the hollow

nanosphere structure is more likely to expose the active sites, promote the interaction between Mn species and Ce species, and thus promote the reaction rate of catalytic combustion of o-DCB. In addition, the relationship between O_{latt} vs T_{90} , T_{50} and E_a is demonstrated in Figs. S4–6. The results show that T_{90} , T_{50} and E_a of $\text{Mn}_2\text{Ce}_1\text{O}_x$ with the best catalytic efficiency are the lowest, while the content of O_{latt} is the highest, which indicates that O_{latt} can promote the catalytic oxidation of o-DCB. In addition, the redox properties of $\text{Mn}_2\text{Ce}_1\text{O}_x$ is the strongest and the acid sites are the most abundant, which indicates that the redox ability and

Table 4Reaction activity of o-DCB elimination over MnCeO_x catalysts.

Catalysts	T ₅₀ ^a (°C)		T ₉₀ ^a (°C)		E _a ^b (kJ/mol)		r ^c (×10 ⁻⁷ mol/(m ² s))		TOF ^d (h ⁻¹)			
	dry	wet	dry	wet	dry	wet	dry	wet	TOF _{Mn}	TOF _{Ce}		
									dry	wet		
MnO_x	345	370	385	420	33.41	41.21	1.94	0.53	0.29	0.08	—	—
$\text{Mn}_2\text{Ce}_1\text{O}_x$	290	310	335	365	27.76	32.30	0.93	0.54	0.28	0.16	2.46	1.39
$\text{Mn}_3\text{Ce}_1\text{O}_x$	310	350	350	400	29.99	40.51	0.48	0.17	0.34	0.12	2.95	1.09

^a The reaction temperature at 50% and 90% o-DCB conversion.^b Activation energies of o-DCB oxidation under o-DCB conversion below 25%.^c Calculated by the conversion of o-DCB at 240 °C.^d TOF is calculated on basis of Mn and Ce species.

acid sites also play an essential role in the catalytic process of o-DCB.

In order to compare the characteristics of intrinsic activity, the kinetics of these MnCeO_x catalysts is analyzed under dry air and 5.0 vol% H_2O conditions, and the reaction rates (r) value of the catalysts is calculated and summarized in Fig. 9e and f and Table 4. Interestingly, under dry air conditions, the r value of MnO_x at 240 °C is 1.94×10^{-7} mol/(m²s) is much higher than that of the r value of $\text{Mn}_2\text{Ce}_1\text{O}_x$ (0.93×10^{-7} mol/(m²s)) and that of $\text{Mn}_3\text{Ce}_1\text{O}_x$ at 240 °C (Fig. 9e and Table 4). In presence 5.0 vol% H_2O we find that the r value of $\text{Mn}_2\text{Ce}_1\text{O}_x$ at 240 °C is 0.54×10^{-7} mol/(m²s) higher than the r value of MnO_x at 240 °C is 0.53×10^{-7} mol/(m²s) higher than $\text{Mn}_3\text{Ce}_1\text{O}_x$ (Fig. 9f and Table 4). In general, the r value of the catalysts at 240 °C under dry air conditions is generally higher than it in the presence of 5.0 vol% H_2O . In order to further explore the difference in activity, taking into account the difference in specific surface area and active species, we also calculated the TOF_{Mn} value of three catalysts and TOF_{Ce} value of $\text{Mn}_3\text{Ce}_1\text{O}_x$ and $\text{Mn}_2\text{Ce}_1\text{O}_x$ under dry air (Fig. 9g and i) and 5.0 vol% H_2O conditions (Fig. 9h and j) (The calculation process showed in the supporting information). The TOF_{Mn} and TOF_{Ce} of these catalysts at 240 °C are also shown in Table 4. It can be found that the TOF_{Mn} value of $\text{Mn}_2\text{Ce}_1\text{O}_x$ catalyst is highest under 5.0 vol% H_2O conditions, slightly lower than MnO_x and $\text{Mn}_3\text{Ce}_1\text{O}_x$ under dry air conditions. The above results show that $\text{Mn}_2\text{Ce}_1\text{O}_x$ hollow nanosphere has good catalytic activity for o-DCB combustion.

3.5.3. Reaction mechanism

The reasonable reaction mechanism of o-DCB combustion

elimination reaction is explored by series characterization, DFT-calculation, selectivity test and catalytic performance under dry air conditions. Specifically, the surface lattice oxygen and the adsorbed oxygen or oxygen vacancy play a vital role in the catalytic oxidation of o-DCB over $\text{Mn}_2\text{Ce}_1\text{O}_x$ catalyst, hence the combustion destruction of o-DCB over $\text{Mn}_2\text{Ce}_1\text{O}_x$ catalyst is consistent with Mars-van Krevelen (MvK) and Langmuir-Hinshelwood (L-H) reaction mechanisms as shown in Fig. 10. In step 1, o-DCB molecule is adsorbed on acid sites (Mn^{4+} , Ce^{3+} or hydroxyl). The C-Cl bond on o-DCB molecule is activated and dissociated by the surface lattice oxygen (in MvK model) and active oxygen (O^- and O_2^-) species (in L-H model), and Cl^- is deposited on cation sites ($\text{Mn}^{4+}/\text{Mn}^{3+}$ and $\text{Ce}^{3+}/\text{Ce}^{4+}$) or oxygen vacancies of MnCeO_x catalyst via nucleophilic substitution. In step 2, the activated and dissociated o-DCB oxidized to primary intermediates (phenols) by surface lattice oxygen or O^- and O_2^- , further to CO_2 and H_2O . The deposited Cl^- ions are finally removed in the form of HCl or Cl_2 , and then the oxygen vacancies are formed. In step 3, gaseous oxygen (O_2) in the environment is activated and oxygen vacancies are supplemented. Therefore, the surface lattice oxygen, active oxygen jointly promote the destruction of o-DCB molecule in this reaction mechanism, which is consistent with our previous work [46].

4. Conclusions

In conclusion, new coronal-like precursors with hollow nanosphere are successfully synthesized by the facile synthetic strategy. Interestingly, the MnO_x derived from Mn-MOFs inherited their micro

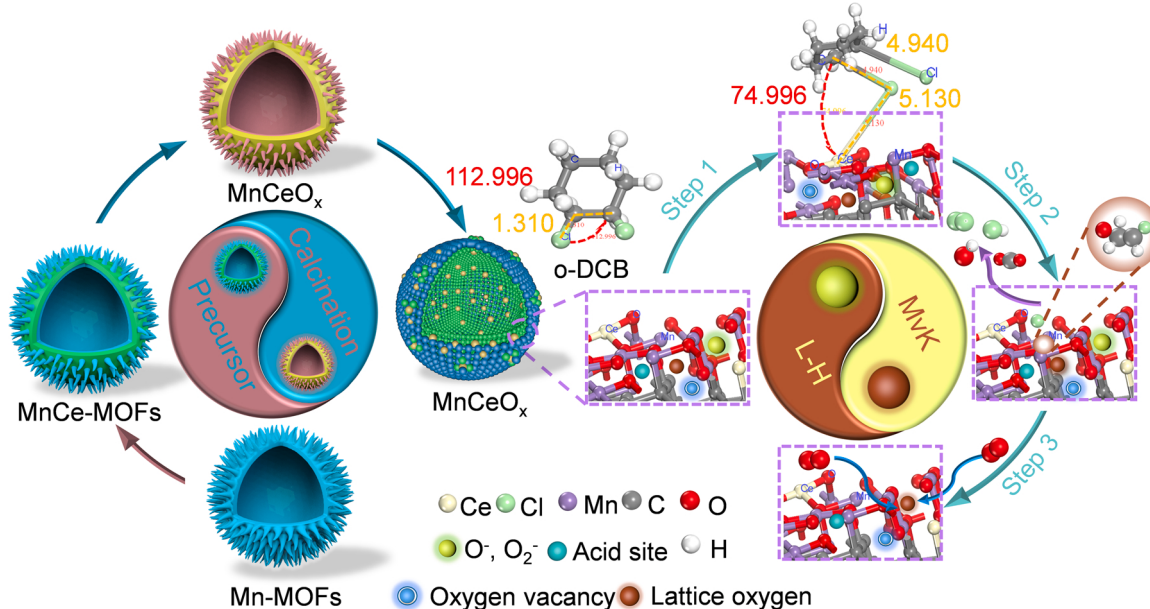


Fig. 10. Possible mechanism in catalytic oxidation reaction of o-DCB over MnCeO_x hollow nanosphere.

morphology. For the o-DCB catalytic oxidation, and the T_{90} of $\text{Mn}_2\text{Ce}_1\text{O}_x$ exhibited satisfactory catalytic performance, which is higher than that of $\text{Mn}_3\text{Ce}_1\text{O}_x$ and MnO_x under dry air and 5.0 vol% H_2O conditions. The interaction between Mn and Ce ($\text{Mn}^{3+} + \text{Ce}^{4+} \rightarrow \text{Mn}^{4+} + \text{Ce}^{3+}$) are presented in MnCeO_x catalysts, which are benefit to the catalytic oxidation of o-DCB. The simulation results of generalized gradient approximation (GGA) of density functional theory (DFT) indicated that the introduction of a certain amount of Ce can effectively improve the adsorption and activation of o-DCB molecules on Mn_3O_4 . The catalytic performance of $\text{Mn}_2\text{Ce}_1\text{O}_x$ is more excellent due to its abundant active sites, strong redox ability and acid sites. Moreover, a combined model of MVK and L-H is proposed on the basis of characterization of O₂-TPD and XPS. The synthetic strategy provides a new idea for the design of hollow microsphere Mn-based catalyst and promotes the application of Mn-based catalyst in o-DCB catalytic oxidation.

CRediT authorship contribution statement

Weitong Ling: Investigation, Methodology, Formal analysis, Writing – original draft. **Peng Gao:** Data curation, Methodology. **Wenyan Du:** Methodology, Resources. **Shilin Wu:** Investigation, Formal analysis. **Haijun Zhao:** Project administration, Writing – review & editing. **Fang Dong:** Conceptualization, Writing – review & editing. **Fei Zha:** Supervision, Conceptualization. **Zhicheng Tang:** Supervision, Funding acquisition.

Declaration of Competing Interest

The authors declare that they have no known competing financial interests or personal relationships that could have appeared to influence the work reported in this paper.

Data availability

The authors do not have permission to share data.

Acknowledgments

The work was financially supported by National Natural Science Foundation of China (52070182), Province Natural Science Foundation of Shandong (ZR2021MB021), Science and Technology Program of Chengguan district (2021–5–2), Youth Innovation Promotion Association CAS (No. 2021421), Major Program of the Lanzhou Institute of Chemical Physics, CAS (No. ZYFZFX-10).

Appendix A. Supporting information

Supplementary data associated with this article can be found in the online version at [doi:10.1016/j.apcatb.2023.122637](https://doi.org/10.1016/j.apcatb.2023.122637).

References

- G. Li, N. Li, Y. Sun, Y. Qu, Z. Jiang, Z. Zhao, J. Cheng, Z. Hao, Efficient defect engineering in Co-Mn binary oxides for low-temperature propane oxidation, *Appl. Catal. B: Environ.* 282 (2021), 119512.
- J. Fu, Z. Zhong, D. Xie, Y. Guo, D. Kong, Z. Zhao, Z. Zhao, M. Li, SERS-active MIL-100(Fe) sensory array for ultrasensitive and multiplex detection of VOCs, *Angew. Chem. Int. Ed.* 59 (2020) 20489–20498.
- F. He, S. Weon, W. Jeon, M. Chung, W. Choi, Self-wetting triphase photocatalysis for effective and selective removal of hydrophilic volatile organic compounds in air, *Nat. Commun.* 12 (2021) 6259.
- C. Liu, X. Chen, H. Chen, Z. Niu, H. Hirao, P. Braunstein, J. Lang, Ultrafast luminescent light-up guest detection based on the lock of the host molecular vibration, *J. Am. Chem. Soc.* 142 (2020) 6690–6697.
- K. Murat, D. Kosuge, J. Ohyam, Y. Mahar, Y. Yamamoto, S. Arai, A. Satsuma, Exploiting metal-support interactions to tune the redox properties of supported Pd catalysts for methane combustion, *ACS Catal.* 10 (2020) 1381–1387.
- M. Cargnello, J. Jaen, J. Garrido, K. Bakhmutsky, T. Montini, J. Gamez, R. Gorte, P. Fornasiero, Exceptional activity for methane combustion over modular Pd@CeO₂ subunits on functionalized Al₂O₃, *Science* 10 (2012) 337.
- H. Zhao, W. Han, Z. Tang, Tailored design of high-stability CoMn_{1.5}O_x@TiO₂ double-wall nanocages derived from prussian blue analogue for catalytic combustion of o-dichlorobenzene, *Appl. Catal. B: Environ.* 276 (2020), 119133.
- W. Huang, X. Zhang, A. Yang, D. Goodman, K. Kao, M. Cargnello, Enhanced catalytic activity for methane combustion through in situ water sorption, *ACS Catal.* 10 (2020) 8157–8167.
- Z. Wang, K. Xie, J. Zheng, S. Zuo, Studies of sulfur poisoning process via ammonium sulfate on MnO₂/γ-Al₂O₃ catalyst for catalytic combustion of toluene, *Appl. Catal. B: Environ.* 298 (2021), 120595.
- D. Yan, S. Mo, Y. Sun, Q. Ren, Z. Feng, P. Chen, J. Wu, M. Fu, D. Ye, Morphology-activity correlation of electrospun CeO₂ for toluene catalytic combustion, *Chemosphere* 247 (2020), 125860.
- J. Zheng, Y. Lu, R. Wang, C. Xie, H. Zhou, S. Jiang, S. Wang, Crystalline TiO₂ protective layer with graded oxygen defects for efficient and stable siliconbased photocathode, *Nat. Commun.* 9 (2018) 3572.
- M. David, L. Pawel, Y. Liu, C. Arata, Y. Tian, K. Kristensen, R. Weber, D. Lunderberg, A. Goldstein, High-resolution exposure assessment for volatile organic compounds in two California residences, *Environ. Sci. Technol.* 55 (2021) 6740–6751.
- H. Deng, S. Ma, L. Wang, C. Zhang, H. He, Role of structural defects in MnO_x promoted by Ag doping in the catalytic combustion of volatile organic compounds and ambient decomposition of O₃, *Environ. Sci. Technol.* 53 (2019) 10871–10879.
- J. Andrey, Y. Zarur, Reverse microemulsion synthesis of nanostructured complex oxides for catalytic combustion, *Nature* 6 (2020) 403.
- S. Wu, H. Zhao, W. Ling, Z. Tang, J. Zhang, In situ self-assembly encapsulation of CoFeO_x nanoparticles in ordered mesoporous TiZrO_x channels for enhanced catalytic combustion of o-dichlorobenzene, *Fuel* 311 (2022), 122496.
- Y. Zhao, C. Deng, D. Tang, L. Ding, Y. Zhang, H. Sheng, H. Ji, W. Song, W. Ma, C. Chen, J. Zhao, α-Fe₂O₃ as a versatile and efficient oxygen atom transfer catalyst in combination with H₂O₂ as the oxygen source, *Nat. Catal.* 4 (2021) 684–691.
- H. Zhao, W. Han, F. Dong, Z. Tang, Highly-efficient catalytic combustion performance of 1,2-dichlorobenzene over mesoporous TiO₂-SiO₂ supported CeMn oxides: The effect of acid sites and redox sites, *J. Ind. Eng. Chem.* 64 (2018) 194–205.
- C. Chen, D. Hong, H. Xia, W. Sun, S. Shao, B. Gong, S. Wang, J. Wu, X. Wang, Q. Dai, Amorphous and homogeneously Zr-doped MnO_x with enhanced acid and redox properties for catalytic oxidation of 1,2-Dichloroethane, *Chem. Eng. J.* 428 (2022), 131427.
- Y. Wang, G. Wang, W. Deng, J. Han, L. Qin, B. Zhao, L. Guo, F. Xing, Study on the structure-activity relationship of Fe-Mn oxide catalysts for chlorobenzene catalytic combustion, *Chem. Eng. J.* 395 (2020), 125172.
- W. Ling, H. Zhao, Z. Tang, F. Zha, Direct synthesis of novel sponge-like porous MnO_x catalysts derived from Mn-MOFs for high-efficiently eliminate o-dichlorobenzene by catalytic combustion, *Catal. Surv. Asia.* 24 (2020) 278–290.
- L. Zhang, W. Deng, Y. Cai, Q. Dai, Q. Guo, L. Comparative studies of phosphate-modified CeO₂ and Al₂O₃ for mechanistic understanding of dichloromethane oxidation and chloromethane formation, *ACS Catal.* 10 (2020) 13109–13124.
- (a) L. Xing, Y. Yang, C. Cao, D. Zhao, Z. Gao, W. Ren, Y. Tian, T. Ding, X. Li, Decorating CeO₂ nanoparticles on Mn₂O₃ nanosheets to improve catalytic soot combustion, *ACS Sustain. Chem. Eng.* 6 (2018) 6544–6554;
(b) X. Li, T. Lunkenbein, V. Pfeifer, M. Jastak, P. Nielsen, F. Girsdsies, A. Knop-Gericke, F. Rosowski, R. Schlogl, A. Trunschke, Selective alkane oxidation by manganese oxide: site isolation of MnO_x chains at the surface of MnWO₄ nanorods, *Angew. Chem. Int. Ed.* 55 (2016) 4092–4096.
- D. Morales, M. Kazakova, S. Dieckhofer, A. Selyutin, G. Golubtsov, W. Schuhmann, J. Masa, Trimetallic Mn-Fe-Ni oxide nanoparticles supported on Multi-Walled carbon nanotubes as high-performance bifunctional ORR/OER electrocatalyst in alkaline media, *Adv. Funct. Mater.* 30 (2020) 1905992.
- X. Qian, X. Han, L. Yu, T. Xu, Y. Chen, Manganese-based functional nanoplatforms: nanosynthetic construction, physiochemical property and theranostic applicability, *Adv. Funct. Mater.* 30 (2020) 1907066.
- J. Yuan, W. Li, S. Gomez, S. Stuib, Shape-controlled synthesis of manganese oxide octahedral molecular sieve three-dimensional nanostructures, *J. Am. Chem. Soc.* 127 (2005) 14184–14185.
- M. Tian, X. Guo, R. Dong, Z. Guo, J. Shi, Y. Yu, M. Cheng, R. Albilali, C. He, Insight into the boosted catalytic performance and chlorine resistance of nanosphere-like meso-macroporous CrO₃/MnCo₃O₄ for 1,2-dichloroethane, *Appl. Catal. B: Environ.* 259 (2019), 118018.
- B. Zhao, Z. Yang, R. Ran, Z. Guo, X. Wu, D. Weng, Fabrication of hollow-structured FeO_x-MnO_x oxidative catalysts with ultra large surface area, *Catal. Commun.* 104 (2018) 13–16.
- Y. Chen, R. Yang, C. Chen, Y. Li, M. Wei, Construction of hierarchical Mn₂O₃ hollow microspheres derived from metal-organic frameworks for high performance supercapacitors, *J. Power Sources* 505 (2021), 230077.
- Q. Dai, K. Shen, W. Deng, Y. Cai, J. Yan, J. Wu, L. Guo, R. Liu, X. Wang, W. Zhan, HCl-tolerant H₃PO₄/RuO_x-CeO₂ catalysts for extremely efficient catalytic elimination of chlorinated VOCs, *Environ. Sci. Technol.* 55 (2021) 4007–4016.
- N. Hanikel, M. Prévot, O. Yaghi, MOF water harvesters, *Nat. Nano.* 15 (2020) 348–355.
- Z. Liu, J. Liu, X. Zhang, Y. Liao, R. Wang, K. Zhang, J. Lyu, O. Farha, J. Hupp, Node-accessible zirconium MOFs, *J. Am. Chem. Soc.* 142 (2020) 21110–21121.
- Y. Wang, H. Jin, Q. Ma, K. Mo, H. Mao, A. Feldhoff, X. Gao, Y. Li, F. Pan, Z. Jiang, A MOF glass membrane for gas separation, *Angew. Chem. Int. Ed.* 59 (2020) 4365–4369.
- W. Ling, H. Zhao, F. Zha, Z. Tang, Precise design and construction of 3D nanoflowers hollow spherical NiO@MnMO_x (M = Co, Cu, and Fe) catalysts for

efficiently catalytic elimination of 1,2-Dichlorobenzene, *Ind. Eng. Chem. Res.* 60 (2020) 14087–14098.

[34] J. Jang, W. Koo, S. Choi, I. Kim, Metal organic framework-templated chemiresistor: sensing type transition from P-to-N using hollow metal oxide polyhedron via galvanic replacement, *J. Am. Chem. Soc.* 139 (2017) 11868–11876.

[35] X. Huang, F. Dong, G. Zhang, Y. Guo, Z. Tang, A strategy for constructing highly efficient yolk-shell Ce@Mn@TiO_x catalyst with dual active sites for low-temperature selective catalytic reduction of NO with NH₃, *Chem. Eng. J.* 419 (2021), 129572.

[36] X. Chen, S. Cai, E. Yu, J. Chen, H. Jia, MnO_x/Cr₂O₃ composites prepared by pyrolysis of Cr-MOF precursors containing *in situ* assembly of MnO_x as high stable catalyst for toluene oxidation, *Appl. Surf. Sci.* 475 (2019) 312–324.

[37] X. Zhang, F. Bi, Z. Zhu, Y. Yang, S. Zhao, J. Chen, X. Lv, Y. Wang, J. Xu, L. Liu, The promoting effect of H₂O on rod-like MnCeO_x derived from MOFs for toluene oxidation: a combined experimental and theoretical investigation, *Appl. Catal. B: Environ.* 297 (2021), 120393.

[38] L. Zhao, Z. Zhang, Y. Li, X. Leng, T. Zhang, F. Yuan, X. Niu, Y. Zhu, Synthesis of Ce_aMnO_x hollow microsphere with hierarchical structure and its excellent catalytic performance for toluene combustion, *Appl. Catal. B: Environ.* 245 (2019) 502–512.

[39] P. Wu, X. Jin, Y. Qiu, D. Ye, Recent progress of thermocatalytic and photo/thermocatalytic oxidation for VOCs purification over manganese-based oxide catalysts, *Environ. Sci. Technol.* 55 (2021) 4268–4286.

[40] Y. Yuan, C. Zhan, K. He, H. Chen, W. Yao, The influence of large cations on the electrochemical properties of tunnel-structured metal oxides, *Nat. Commun.* 7 (2016) 13374.

[41] Y. Mu, X. Huang, Z. Tang, Q. Wang, Ordered mesoporous TiO₂ framework confined CeSn catalyst exhibiting excellent high activity for selective catalytic reduction of NO with NH₃ at low temperature, *Chem. Eng. J.* 454 (2023), 140181.

[42] Y. Wang, S. Aghamohammadi, D. Li, K. Li, R. Farrautoa, Structure dependence of Nb₂O₅_x supported manganese oxide for catalytic oxidation of propane: Enhanced oxidation activity for MnO_x on a low surface area Nb₂O₅_x, *Appl. Catal. B: Environ.* 244 (2019) 438–447.

[43] P. Zhang, H. Lu, Y. Zhou, L. Zhang, Z. Wu, S. Yang, H. Shi, Q. Zhu, Y. Chen, S. Dai, Mesoporous MnCeO_x solid solutions for low temperature and selective oxidation of hydrocarbons, *Nat. Commun.* 6 (2015) 8446.

[44] Y. Duan, Y. Zhou, Y. Zhen, D. Liu, Z. Wen, J. Yan, Q. Jiang, Q. Boosting production of HCOOH from CO₂ electroreduction via Bi/CeO_x, *Angew. Chem. Int. Ed.* 60 (2021) 8798–8802.

[45] R. Singh, E. Davydova, J. Douglin, A. A. Godoy, H. Tan, M. Bellini, B. Allen, J. Jankovic, H. Miller, A. Alba-Rubio, D. Dekel, Synthesis of CeO_x-Decorated Pd/C catalysts by controlled surface reactions for hydrogen oxidation in anion exchange membrane fuel cells, *Adv. Funct. Mater.* 30 (2020) 2002087.

[46] W. Ling, H. Zhao, S. Wu, Z. Tang, F. Zha, A CeCoO_x Core/Nb₂O₅@TiO₂ double-shell nanocage catalyst demonstrates high activity and water resistance for catalytic combustion of o-Dichlorobenzene, *Chem. -Eur. J.* 27 (2021) 10356–10368.

[47] Y. Huang, S. Zhang, X. Lu, Z. Wu, D. Luan, D. Lou, X. Trimetallic spinel NiCo₂_xFe₂O₄ nanoboxes for highly efficient electrocatalytic oxygen evolution, *Angew. Chem. Int. Ed.* 60 (2021) 11841–11846.

[48] H. Sun, X. Yu, X. Ma, X. Yang, M. Lin, M. Ge, MnO_x-CeO₂ catalyst derived from metal-organic frameworks for toluene oxidation, *Catalysis* 355 (2020) 580–586.

[49] X. Yang, X. Yu, M. Jing, W. Song, J. Liu, M. Ge, Defective Mn_xZr_{1-x}O₂ solid solution for the catalytic oxidation of toluene: insights into the oxygen vacancy contribution, *ACS Appl. Mater. Interfaces* 11 (2019) 730–739.

[50] S. Jiang, C. Li, Y. Mohammad, Y. Tang, R. Wang, J. Li, Z. Zhao, Z. Zhao, Solvent-induced fabrication of Cu/MnO_x nanosheets with abundant oxygen vacancies for efficient and long-lasting photothermal catalytic degradation of humid toluene vapor, *Appl. Catal. B: Environ.* 328 (2023), 122509.

[51] G. Long, M. Chen, Y. Li, J. Ding, R. Sun, Y. Zhou, X. Huang, G. Han, W. Zhao, One-pot synthesis of monolithic Mn-Ce-Zr ternary mixed oxides catalyst for the catalytic combustion of chlorobenzene, *Chem. Eng. J.* 360 (2019) 964–973.

[52] M. Sun, Y. Peng, Study on structural electronic and magnetic properties of Sn atom adsorbed on defective graphene by first-principle calculations, *Appl. Surf. Sci.* 307 (2014) 158–164.

[53] T. Cai, H. Huang, W. Deng, Q. Dai, W. Liu, X. Wang, Catalytic combustion of 1,2-dichlorobenzene at low temperature over Mn-modified Co₃O₄ catalysts, *Appl. Catal. B-Environ.* 166–167 (2015) 393–405.

[54] W. Deng, Q. Dai, Y. Lao, B. Shi, X. Wang, Low temperature catalytic combustion of 1,2-dichlorobenzene over CeO₂-TiO₂ mixed oxide catalysts, *Appl. Catal. B-Environ.* 181 (2016) 848–861.

[55] S. Yang, H. Zhao, F. Dong, F. Zha, Z. Tang, Highly efficient catalytic combustion of o-dichlorobenzene over three-dimensional ordered mesoporous cerium manganese bimetallic oxides: a new concept of chlorine removal mechanism, *Mol. Catal.* 463 (2019) 119–129.

[56] S. Wu, H. Zhao, Z. Tang, J. Zhang, Controlled synthesis of ordered mesoporous TiO₂-ZrO₂ supported CeSn oxides catalyst for the elimination of 1,2-dichlorobenzene, *Micro Mesopor. Mater.* 302 (2020), 110214.

[57] Y. Gu, S. Shao, W. Sun, H. Xia, X. Gao, Q. Dai, The oxidation of chlorinated organic compounds over W-modified Pt/CeO₂ catalysts, *J. Catal.* 380 (2019) 375–386.

[58] A. Tang, L. Hu, X. Yang, Y. Jia, Y. Zhang, Promoting effect of the addition of Ce and Fe on manganese oxide catalyst for 1,2-dichlorobenzene catalytic combustion, *Catal. Commun.* 82 (2016) 41–45.

[59] X. Ma, H. Sun, Q. Sun, X. Feng, H. Guo, B. Fan, Catalytic oxidation of CO and o-DCB over CuO/CeO₂ catalysts supported on hierarchically porous silica, *Catal. Commun.* 12 (2011) 426–430.

[60] X. Ma, Q. Sun, X. Feng, X. He, J. Guo, H. Sun, Catalytic oxidation of 1,2-dichlorobenzene over CaCO₃- α -Fe₂O₃ nanocomposite catalysts, *Appl. Catal. A Gen.* 450 (2013) 143–151.